Chapter 4
Calcium Waves and Sparks

Calcium (Ca^{2+}) is one of the most important and well-studied cellular signaling molecules. From a modeling perspective, it attracts a great deal of interest due to the fact that calcium signaling often involves complex spatiotemporal dynamics, including oscillations and waves. There are a number of excellent general reviews on the modeling of calcium dynamics within cells, including Chap. 7 of Keener and Sneyd [322] and Falcke [181]. In this chapter, we focus on the mathematical modeling and analysis of calcium waves and their potential significance in neuronal calcium signaling; see also the reviews by Berridge [43] and Ross [534]. Although there are a number of very detailed whole-cell models of calcium signaling, we will focus on simplified models that are analytically tractable. In particular, we will highlight some of the mathematical methods used to characterize calcium waves.

4.1 Calcium Signaling in Neurons

In vertebrates, most of the Ca^{2+} is stored in bones, from where it can be released by hormonal stimulation to maintain a high extracellular Ca^{2+} concentration (around 1 mM). On the other hand, active ion pumps and exchangers maintain the cytoplasmic Ca^{2+} concentration at relatively low levels (around 10–100 nM). The resulting steep concentration gradient across the plasma membrane means that cells are able to increase their cytoplasmic Ca^{2+} concentration rapidly by opening either voltage-gated or ligand-gated Ca^{2+} ion channels. Within the context of neuronal processing, the activation of voltage-gated calcium channels (VGCCs) at axon terminals triggers the release of synaptic neurotransmitter (see Sect. 1.3); VGCCs also contribute to the generation of dendritic action potentials (see Sects. 1.4.3 and 3.1). A classical example of ligand gating in neurons is the entry of Ca^{2+} through NMDA receptors on postsynaptic dendritic spines. The resulting transient Ca^{2+} signal is thought to play a major role in the induction of changes in synaptic strength; see below.

Another major mechanism whereby cells, including neurons, regulate their cytoplasmic Ca^{2+} concentration is via the intracellular supply of Ca^{2+} from internal

P.C. Bressloff, *Waves in Neural Media: From Single Neurons to Neural Fields*,
Lecture Notes on Mathematical Modelling in the Life Sciences,
DOI 10.1007/978-1-4614-8866-8_4,

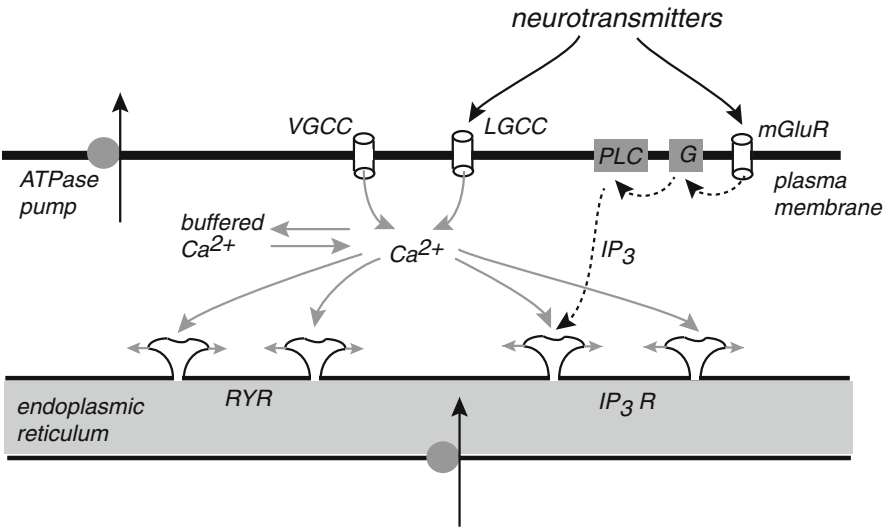

Fig. 4.1 Neural calcium signaling. The entry of Ca^{2+} from outside the cell is mediated by voltage-gated (VGCC) and ligand-gated (LGCC) calcium channels. Stimulation of metabotropic glutamate receptors (mGluRs) produces IP_3 second messengers that bind to IP_3 receptors (IP_3Rs), which subsequently release Ca^{2+} from the endoplasmic reticulum. Both IP_3Rs and Ryanodine receptors (RyRs) are sensitive to Ca^{2+}, resulting in Ca^{2+}-induced Ca^{2+}-release (CICR). The latter can sometimes result in the propagation of a Ca^{2+} wave along the dendrites

stores such as the *endoplasmic reticulum* (ER) and *mitochondria*. *Inositol (1,4,5)-trisphosphate* (IP_3) receptors and *Ryanodine* (Ry) receptors distributed throughout the ER, for example, mediate the release of Ca^{2+} into the cytoplasm, whereas Ca^{2+} ion pumps maintain the relatively high Ca^{2+} concentration within the ER. The Ry receptor plays a critical role in excitation–contraction coupling in skeletal and cardiac muscle cells, but is also found in nonmuscle cells such as neurons. One important feature of Ry receptors is that they can undergo Ca^{2+}-induced Ca^{2+}-release (CICR), in which elevated cytoplasmic Ca^{2+} activates Ry receptors that release further Ca^{2+}, which then activates other Ry receptors, resulting in a nonlinear regenerative feedback mechanism. The IP_3 receptor is similar in structure to the Ry receptor, but is found predominantly in nonmuscle cells and is sensitive to the second messenger IP_3. The binding of an extracellular ligand such as a hormone or a neurotransmitter to a metabotropic receptor results in the activation of a G-protein and the subsequent activation of phospholipase C (PLC). This then cleaves phosphatidylinositol bisphosphate (PIP_2) into diacylglycerol (DAG) and IP_3. The water soluble IP_3 is free to diffuse throughout the cell cytoplasm and bind to IP_3 receptors located on the ER membrane, which then open and release Ca^{2+} from the ER. The opening and closing of an IP_3 receptor is also modulated by the concentration of cytoplasmic Ca^{2+}, so it too can undergo CICR. Yet another mechanism for controlling cytoplasmic Ca^{2+} is through buffering (binding) to large proteins. Indeed, it is estimated that

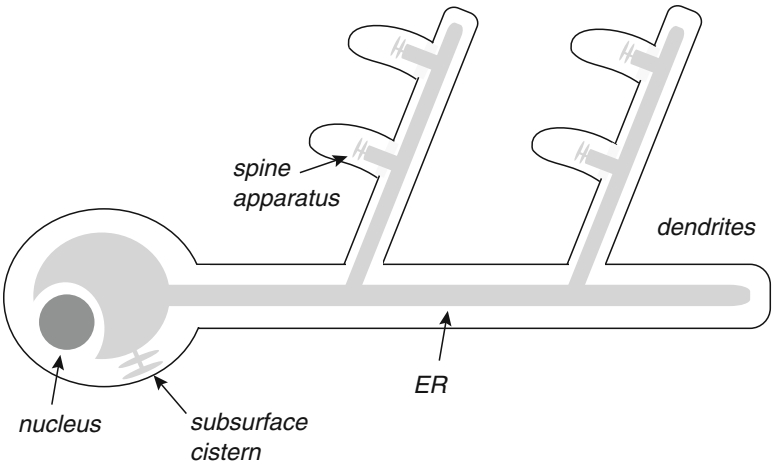

Fig. 4.2 The endoplasmic reticulum (ER) is a single and continuous membrane-bound organelle that is distributed throughout the dendrites and axon (not shown) of a neuron [516]. It is responsible for the synthesis and posttranslational modification of most secretory and membrane proteins, as well as the regulation of Ca^{2+} levels. The shape of the ER is heterogeneous, but can be divided into three domains: the nuclear envelope, the ribosome-bound rough ER (RER), and the ribosome-free smooth ER (SER). The RER is constituted primarily by sheets or cisternae, whereas the SER is predominantly composed of 60–100 nm diameter tubules that form irregular polygons with a common luminal space connected via three-way junctions. The ER present in the soma and proximal dendritic compartment is rich in ribosomes, corresponding to the RER, whereas the ER distributed in distal dendrites and axons corresponds mostly to SER and contains only a few sparse ribosomes. The ER comes into close proximity with the plasma membrane at various locations, forming subsurface cisternae within the soma and axon initial segment, and the spine apparatus within dendritic spines

at least 99 % of the total cytoplasmic Ca^{2+} is bound to buffers. A summary of the basic extracellular and intracellular mechanisms for controlling the concentration of cytoplasmic Ca^{2+} is shown in Fig. 4.1.

The signaling mechanisms and dynamics of Ca^{2+} release from the ER in neurons have been much less well studied than extracellular sources of Ca^{2+}. However, the ER is a continuous network that is distributed throughout a neuron, extending all the way into the dendrites and axon and coming into close contact with the plasma membrane and synapses at many locations; see Fig. 4.2. Hence, as suggested by Berridge [43], it is likely that the integrative and regenerative properties of the ER and plasma membrane provide a binary membrane system that regulates a variety of neuronal process via Ca^{2+} signaling, including excitability, neurotransmitter release, synaptic plasticity, and gene transcription.

(a) Within the soma and initial axonal segment, the ER forms flattened sheets known as *subsurface cisternae* that come into close contact with the plasma membrane. These internal structures are thought to play an important role in regulating neuronal excitability. For example, many neurons exhibit significant after-hyperpolarizations (AHPs) following either a single action potential or a

burst of action potentials, which suppress subsequent firing of the cell (spike frequency adaptation). Often AHPs have both a fast component and a slow component, which arise from the opening of two separate Ca^{2+}-activated K^+ channels (gK_{Ca1} and gK_{Ca2}). The fast activation of gK_{Ca1} is due to the entry of extracellular Ca^{2+} via VCCNs during the course of an action potential, whereas the slow activation of gK_{Ca2} is probably due to CICR from Ry receptors located in the subsurface cisternae.

(b) Within the axon, the ER consists of connecting tubules that run parallel along the axon. The axonal ER network extends into a synapse, coming into close contact with the plasma membrane and associated neurotransmitter secretory vesicles. It is thought that calcium release from Ry and IP_3 receptors contributes to the formation of localized high-concentration bursts of Ca^{2+} necessary for the exocytosis (transport and fusion) of vesicles to the plasma membrane.

(c) The ER network is also distributed throughout the dendritic tree and into spines, where it terminates at the so-called spine apparatus. The latter consists of closely packed plates of ER that are located within the middle of the spine and is thus well placed to contribute to Ca^{2+} signaling during synaptic plasticity. The latter refers to the rapid and long-lasting changes in synaptic strength that are thought to provide the subcellular substrate for learning and memory. Much of the information regarding synaptic plasticity in mammalian neurons has been obtained from studies of hippocampal and cerebellar neurons [120, 123, 385, 402]. In particular, it has been found that the same synapses can be switched rapidly and reversibly from an enhanced state of *long-term potentiation* (LTP) to a reduced state of *long-term depression* (LTD). Interestingly, both LTP and LTD are induced by a transient increase in the local Ca^{2+} concentration within a spine. It was originally thought that the bidirectional switch only depended on the amplitude of the Ca^{2+} signal, with a stronger stimulus inducing LTP and a weaker one LTD. Now, however, it appears likely that the detailed spatial and temporal structure of the calcium signal may be important. Although the influx of extracellular Ca^{2+} through NMDA receptors or voltage-gated channels is still the major contributor to the induction of LTP and LTD, there is increasing evidence that there is also a component arising from intracellular stores [428, 447, 534]. Activation of the ER could be mediated either by Ca^{2+} itself via CICR or by stimulation of metabotropic glutamate (mGlu) receptors in the plasma membrane, resulting in the production of IP_3. The fact that CICR requires both cytoplasmic IP_3 and Ca^{2+} suggests that IP_3 receptors could act as *coincidence detectors* for mGluR activation and postsynaptic Ca^{2+} signaling arising from back-propagating action potentials or dendritic Ca^{2+} spikes [658].

(d) One of the most dramatic consequences of CICR is the propagation of intracellular Ca^{2+} waves mediated primarily by the opening of IP_3 receptors. These waves were first observed in nonneuronal cells such as *Xenopus laevis* oocytes [367, 490], where the resulting changes in Ca^{2+} concentration across the whole cell provided a developmental signal. The discovery of Ca^{2+} waves in neurons is more recent [303, 428, 447, 534, 658]. Since these cells have extensive den-

dritic and axonal arborizations, the distribution of the components of the Ca^{2+} signaling apparatus within the cell plays a crucial role in determining whether or not local Ca^{2+} release transforms into a propagating wave, and how far it travels. For example, in pyramidal neurons of the hippocampus and cortex, Ca^{2+} waves are usually observed in the primary apical dendrite and perhaps the soma, rarely reaching beyond the point where thick dendrites begin to branch. Since the ER network is distributed throughout the cell, this suggests that there is a heterogeneous distribution of mGlu receptors and IP_3 receptors along the dendrite. Ca^{2+} waves rarely propagate from the dendrite to the soma, unless there is a sufficiently strong and sustained stimulation of a neuron that results in high levels of cytoplasmic IP_3 or higher concentrations of internally stored Ca^{2+}. If a Ca^{2+} wave did reach the soma, then it would generate a strong Ca^{2+} signal in the soma and nucleus due to the high concentration of IP_3 receptors in these regions. It has been suggested that a Ca^{2+} wave could allow a strongly stimulated synapse in the dendrites to signal to the nucleus, where the large increase in Ca^{2+} concentration could activate gene transcription, which is a necessary step in more persistent forms of synaptic plasticity such as late long-term potentiation (L-LTP). However, the role of Ca^{2+} waves in initiating gene transcription is still controversial. On the other hand, the likely contribution of IP_3 receptor-mediated Ca^{2+} release during normal LTP and LTD indicates that Ca^{2+} waves could be important in determining the spatiotemporal pattern of synaptic changes.

(e) Many nonneuronal cell types exhibit spontaneous localized Ca^{2+} release events known as *sparks* [110]. Calcium sparks, which are thought to be the building blocks of the large regenerative Ca^{2+} signal that controls contraction in cardiac and skeletal muscle cells, arise from the opening of clusters of RyRs by local CICR. The frequency of calcium spark events is sensitive to changes in membrane potential, although they rarely induce calcium waves [111]. Similar events known as calcium *puffs* have been found in *Xenopus laevis* oocytes [489, 490, 690]. They are also spatially and temporally localized, are fast, and occur stochastically. However, in contrast to sparks, they are mediated by IP_3Rs and coalesce more easily to form calcium waves. Localized events in neurons with spark-like and puff-like properties have recently been observed in slice preparations, and their frequency can be modulated by synaptic activity and changes in membrane potential [389, 403]. Although it is likely that they also occur in vivo, it is not yet clear whether or not they have a specific function.

4.2 Reaction–Diffusion Models of Ca^{2+} Dynamics

One of the major challenges in modeling calcium waves is that the ER and cytoplasm comprise two highly interconnected three-dimensional domains (ignoring, for simplicity, other intracellular compartments such as the mitochondria). Assuming

that Ca^{2+} undergoes normal diffusion within each compartment, together with buffering, we can write down the following pair of diffusion equations for the Ca^{2+} concentrations c, c_e in the cytoplasm and ER [322]:

$$\frac{\partial c}{\partial t} = \nabla \cdot (D_c \nabla c) - J_{\text{on}} + J_{\text{off}}, \quad \mathbf{r} \in \Omega_c \tag{4.1}$$

and

$$\frac{\partial c_e}{\partial t} = \nabla \cdot (D_e \nabla c_e) - \hat{J}_{\text{on}} + \hat{J}_{\text{off}}, \quad \mathbf{r} \in \Omega_e, \tag{4.2}$$

where Ω_c and Ω_e denote the cytoplasmic and ER domains, respectively, D_c and D_e are the corresponding diffusivities in the two domains, and the on/off fluxes take into account the binding/unbinding of Ca^{2+} to buffering proteins. These equations are supplemented by various boundary conditions that take into account the exchange of Ca^{2+} between the cytoplasm and the plasma membrane or ER. Let J_{in} denote the total inward flux of Ca^{2+} from the plasma membrane to the cytoplasm via voltage-gated and ligand-gated ion channels, and let J_{p1} be the outward flux due to ATPase ion pumps in the plasma membrane. Then

$$D_c \nabla c \cdot \mathbf{n} = J_{\text{in}} - J_{\text{p1}}, \quad \mathbf{r} \in \partial\Omega_{c,m}, \tag{4.3}$$

where $\partial\Omega_{c,m}$ is the surface of the plasma membrane with unit normal $\mathbf{n}$. Similarly, let J_{IP} and J_{Ry} denote the inward fluxes from the ER to the cytoplasm via IP_3Rs and RyRs, respectively, and let J_{p2} denote the outward flux due to ion pumps in the ER. This yields

$$D_c \nabla c \cdot \hat{\mathbf{n}} = -D_e \nabla c_e \cdot \hat{\mathbf{n}} = J_{\text{IP}} + J_{\text{Ry}} - J_{\text{p2}}, \quad \mathbf{r} \in \partial\Omega_e, \tag{4.4}$$

where $\partial\Omega_e$ is the boundary of the ER with unit normal $\hat{\mathbf{n}}$. A schematic diagram of all the fluxes is shown in Fig. 4.3.

Let us first consider a space-clamped version of this model, in which one treats the cytoplasm and ER as two well-mixed homogeneous compartments. In that case, the various surface and volume fluxes are combined as follows:

$$\frac{dc}{dt} = -J_{\text{on}} + J_{\text{off}} + \frac{|\partial\Omega_{c,m}|}{|\Omega_c|}[J_{\text{in}} - J_{\text{p1}}] + \frac{|\partial\Omega_e|}{|\Omega_c|}[J_{\text{IP}} + J_{\text{Ry}} - J_{\text{p2}}] \tag{4.5}$$

and

$$\frac{dc_e}{dt} = -\hat{J}_{\text{on}} + \hat{J}_{\text{off}} - \frac{|\partial\Omega_e|}{|\Omega_e|}[J_{\text{IP}} + J_{\text{Ry}} - J_{\text{p2}}]. \tag{4.6}$$

Each of the fluxes in these equations corresponds to a component of the so-called Ca^{2+}-signaling toolkit [44]. Thus, the equations for Ca^{2+} dynamics have to be coupled to additional biochemical equations describing the dynamics of ion pumps, the Ca^{2+}-dependent gating of the Ry and IP_3 receptors, and how the latter are regulated by the second messenger IP_3. Often the external flux J_{in} is simply taken to be a linear increasing function of the IP_3 concentration. There have been many studies of space-clamped Ca^{2+} models with particular focus on calcium oscillations

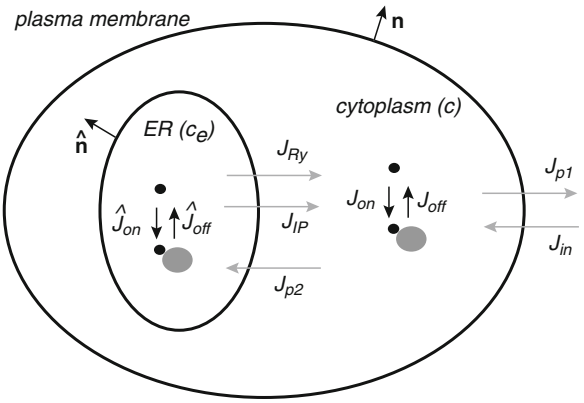

Fig. 4.3 Schematic diagram showing various fluxes in reaction–diffusion model of Ca^{2+} dynamics

[181, 322]. Although the models differ in their degree of complexity with regards the component fluxes, they can often be reduced to simpler models that have similar structure to the FitzHugh–Nagumo (FN) model of excitability. For example, suppose that we ignore fluxes through the plasma membrane so that the total intracellular Ca^{2+} is conserved, that is, $|\Omega_c|c + |\Omega_e|c_e$ is a constant. Furthermore, suppose that there are only two intracellular fluxes, $J_{\rm IP}$ and $J_{\rm p2}$, and the IP_3 concentration is fixed. Ignoring the effects of buffering, one can write down an analogous equation to (2.3) of the form

$$\frac{dc}{dt} = f(c,h), \quad \tau(c)\frac{dh}{dt} = h_\infty(c) - h, \tag{4.7}$$

where c is the concentration of free cytosolic Ca^{2+}, $f(c,h)$ represents the net flux into the cytoplasm from the ER, and h is an inactivation variable that plays a similar role to the recovery variable w of the original FN equations. One interpretation of h is the fraction of IP_3 receptors that are not inactivated by bound Ca^{2+}. Li and Rinzel [381] derived such a two-variable model by reducing the classical kinetic model of Ca^{2+}-gated IP_3 receptors due to De Young and Keizer [692]; see Sect. 4.4.1.

Unfortunately, the complex geometry and heterogeneity of the ER means that the spatially distributed model given by (4.1)–(4.4) is far too complicated to analyze, even when simplified models of the various fluxes are considered. A common strategy is to ignore the detailed structure of the ER by assuming that the concentrations c and c_e coexist at every point in space. This is motivated by the idea that since diffusion is fast over short distances, local variations due to heterogeneities are smoothed out. Phenomenologically speaking, this leads to the *calcium bidomain equations*

$$\frac{\partial c}{\partial t} = \nabla\cdot(\overline{D}_c\nabla c) - J_{\rm on} + J_{\rm off} + \chi_c[J_{\rm IP} + J_{\rm Ry} - J_{\rm p2}] \tag{4.8}$$

and

$$\frac{\partial c_e}{\partial t} = \nabla \cdot (\overline{D}_e \nabla c_e) - \hat{J}_{\rm on} + \hat{J}_{\rm off} - \chi_e [J_{\rm IP} + J_{\rm Ry} - J_{\rm p2}]. \tag{4.9}$$

Here $\chi_c = |\partial\Omega_e|/|\Omega_c|, \chi_e = |\partial\Omega_e|/|\Omega_e|$ are surface to volume ratios, and $\overline{D}_c, \overline{D}_e$ are effective diffusion coefficients. Note, however, that in order to determine the effective diffusion coefficients, which will depend on the geometry of the ER, and justify the precise form of the factors χ_c, χ_e, it is necessary to derive these equations from first principles using homogenization theory [224, 322]. Elements of the theory are described in appendix section 4.6. Now suppose that only the fluxes $J_{\rm IP}$ and $J_{\rm p2}$ are included along the lines of the space-clamped model. However, in contrast to the latter, it is now necessary to keep track of both the cytoplasmic and ER Ca^{2+} concentrations, since they are spatially varying. A one-dimensional bidomain model with constant diffusion coefficients then takes the form

$$\frac{\partial c}{\partial t} = D_c \frac{\partial^2 c}{\partial x^2} + f(c, c_e, h) \tag{4.10a}$$

$$\frac{\partial c_e}{\partial t} = D_e \frac{\partial^2 c}{\partial x^2} - \chi_e f(c, c_e, h) \tag{4.10b}$$

$$\tau(c) \frac{\partial h}{\partial t} = h_\infty(c) - h, \tag{4.10c}$$

where $f(c, c_e, h)$ represents the net Ca^{2+} flux from the ER to the cytoplasm the spatial dimensions have been fixed such that $\chi_c = 1$. Analysis of traveling wave solutions of (4.10) proceeds along very similar lines to that of the Hodgkin–Huxley equations for membrane voltage excitability; see Chap. 2. Depending on parameter values, the model system can support solitary waves when the physiological state of the cytoplasm is excitable, periodic waves when it is oscillatory, and traveling fronts when it is bistable [322].

However, one important feature that needs to be taken into account in the case of calcium excitability is buffering. Insights into the effects of buffering can be obtained by looking at reduced models of excitability such as the bistable equation or the FN equations [592, 635, 636, 653]. Following [592, 653], consider a simple extension of the bistable equation (Sect. 2.2). First, note that the basic chemical reaction for Ca^{2+} buffering takes the form

$$P + {\rm Ca}^{2+} \underset{k_-}{\overset{k_+}{\rightleftharpoons}} B,$$

where P is the buffering protein and B is the protein/Ca^{2+} complex. Let c and b denote, respectively, the concentration of free cytosolic Ca^{2+} and buffered Ca^{2+}. The extended bistable equation is then (in one spatial dimension)

$$\frac{\partial c}{\partial t} = D_c \frac{\partial^2 c}{\partial x^2} + f(c) + k_- b - k_+ c(b_t - b), \tag{4.11a}$$

$$\frac{\partial b}{\partial t} = D_b \frac{\partial^2 b}{\partial x^2} - k_- b + k_+ c(b_t - b). \tag{4.11b}$$

Here b_t is the total buffer concentration, $f(c)$ takes into account all Ca^{2+} fluxes, and the diffusion coefficients of free and buffered Ca^{2+} are assumed to be constants. Suppose that the buffer reaction rates $k_\pm$ are faster than the time constants of Ca^{2+} dynamics. The buffer concentration b can be taken to be in the quasi steady state $k_- b - k_+ c(b_t - b) = 0$, that is,

$$b = \frac{b_t c}{K + c}, \quad K = \frac{k_-}{k_+}. \tag{4.12}$$

Adding (4.11a) and (4.11b) and eliminating b using (4.12) gives [653]

$$\begin{aligned}\frac{\partial c}{\partial t} &= \frac{1}{1+\theta(c)}\left(\frac{\partial^2 w(c)}{\partial x^2} + f(c)\right) \\ &= \frac{D_c + D_b\theta(c)}{1+\theta(c)}\frac{\partial^2 c}{\partial x^2} - \frac{2D_b\theta(c)}{(K+c)(1+\theta(c))}\left(\frac{\partial c}{\partial x}\right)^2 + \frac{f(c)}{1+\theta(c)},\end{aligned}$$

where

$$w(c) = D_c c + D_b b_t \frac{c}{K+c}, \quad \theta(c) = \frac{b_t K}{(K+c)^2}. \tag{4.13}$$

It is clear that a mobile buffer ($D_b > 0$) generates a nonlinear advection–diffusion equation for c; the advection term vanishes if the buffer is immobile ($D_b = 0$).

The form of the effective reaction–diffusion equation for c suggests making then change of variables $w = w(c)$, with w, a monotone increasing function of c since $w'(c) = D_c + D_b\theta(c) > 0$. Denoting the unique inverse of the function $w(c)$ by $c = \phi(w)$, we can write

$$\frac{\partial w}{\partial t} = \frac{D_c + D_b\Theta(w)}{1+\Theta(w)}\left(\frac{\partial^2 w}{\partial x^2} + f(\phi(w))\right), \tag{4.14}$$

where $\Theta(w) = b_t K/(K+\phi(w))^2$. Now suppose that $f(c)$ has two stable zeros $c_\pm$ separated by an unstable zero c_0 with $c_- < c_0 < c_+$. It immediately follows that $f(\Theta(w))$ has three corresponding zeros $w_\pm, w_0$ with $w_- < w_0 < w_+$ and $w_\pm$ stable. A traveling front solution of wave speed v, $w(x,t) = W(x - vt)$, satisfies the ODE

$$V_{\xi\xi} + \frac{v}{D_{eff}(W)}W_\xi + f(\phi(W)). \tag{4.15}$$

Proceeding as in Sect. 2.2, multiply both sides of this equation by W_ξ and integrate to show that

$$v\int_{-\infty}^{\infty} \frac{W_\xi^2}{D_{\text{eff}}(W(\xi))}d\xi = \int_{w_-}^{w_+} f(\phi(w))dw.$$

Since the integral on the left-hand side is positive definite, the sign of v is determined by the sign of the integral on right-hand side. In particular, a right-moving wave ($v > 0$) exists provided that

$$\int_{c_-}^{c_+} (D_c + D_b\theta(c))\, f(c)dc > 0, \tag{4.16}$$

where we have converted back to the original variable c. It can be seen that immobile buffers ($D_b = 0$) have no effect on the existence of a traveling wave; this result also holds true for wave stability and uniqueness. On the other hand, mobile buffers can eliminate a traveling wave when they are of high affinity (small K) or have a large diffusion coefficient (large D_b).

4.3 Discrete Calcium Sources and the Fire–Diffuse–Fire Model

4.3.1 Discrete Calcium Sources and Averaging

The above reaction–diffusion models assumed that Ca^{2+} release from the ER is homogeneous in space. This neglects the fact that IP_3 receptors (as well as Ry receptors) tend to be arranged in clusters. For example, in *Xenopus* oocytes, the density of clusters is around 1 per $30\,\mu m^2$, with each cluster containing about 25 IP_3 receptors [322]. Consequently, the propagation of Ca^{2+} waves tends to be saltatory, jumping from one cluster to the next. (Clustering of IP_3 receptors is also thought to occur along dendrites [534]). We have previously encountered saltatory waves due to discreteness effects, namely, action potential propagation along myelinated axons (Sect. 2.5) and solitary Ca^{2+} spikes propagating along spiny dendrites (Sect. 3.1). The latter waves depend on the action of VGCCs and other voltage-gated ion channels and are thus distinct from the Ca^{2+} waves considered in this chapter, which depend on Ca^{2+} release from internal pools. Nevertheless, the analytical techniques used to study these other examples can be adapted to the present case. First, we will discuss how the averaging method of Sect. 2.5 can be used to study wave propagation failure in the presence of discrete release sites, following [318]. We will then describe an alternative, *fire–diffuse–fire* (FDF) model of saltatory Ca^{2+} waves, which is identical in structure to the spike–diffuse–spike (SDS) model of Sect. 3.1. (In contrast to other chapters, we will use c to denote cytosolic Ca^{2+} concentration and v to denote wave speed.)

Consider a one-dimensional model of Ca^{2+} diffusion and release of the form [318]

$$\frac{\partial c}{\partial t} = -k_c c + D_c \frac{\partial^2 c}{\partial x^2} + L \sum_n \delta(x - nL) f(c), \tag{4.17}$$

where $f(c)$ represents the Ca^{2+}-dependent rate of release from each cluster (taken to be identical), and the decay term represents the effects of ion pumps. The clusters are assumed to be evenly spaced with spatial separation L. For simplicity, the ER concentration c_e and IP_3 concentration p are taken to be fixed. It is tempting to apply homogenization theory to this problem (see appendix section 4.6), assuming diffusion is fast on the length scale L, that is, $L^2 k_c / D_c \ll 1$. Intuitively, one would expect the L-periodic function $g(x) = L \sum_n \delta(x - nL)$ to be replaced by its spatial average $\int_0^L g(x)dx/L = 1$. However, as highlighted by Keener [318, 319] and discussed in Sect. 2.5, the homogenized system cannot account for the fact that discreteness

effects can lead to wave propagation failure in regimes that the continuous model would predict traveling waves exist. This reflects the fact that wave solutions are not structurally stable. The occurrence of propagation failure can be established by constructing standing wave-front solutions [318, 322]. The latter are stationary solutions of (4.17). On the intervals $nL < x < (n+1)L$, this gives

$$0 = -k_c c + D_c \frac{\partial^2 c}{\partial x^2}, \tag{4.18}$$

which is supplemented by jump conditions at $x = nL$,

$$D_c \frac{\partial c}{\partial x}\Big|_{nL_-}^{nL_+} + Lf(c_n) = 0. \tag{4.19}$$

The latter is obtained by integrating the stationary equation on either side of $x = nL$. The general solution of (4.18) is

$$c(x) = c_n \cosh(\beta(x-nL)/L) + \hat{c}_n \sinh(\beta(x-nL)/L), \quad nL < x < (n+1)L,$$

where $\beta^2 = k_c L^2/D_c$, $c_n = c(nL)$ and $\beta \hat{c}_n/L = c'(nL_+)$. Continuity of the solution at $x = (n+1)L$ shows that

$$c_n \cosh(\beta) + \hat{c}_n \sinh(\beta) = c_{n+1},$$

that is,

$$\hat{c}_n = \frac{c_{n+1} - c_n \cosh(\beta)}{\sinh(\beta)}.$$

It follows that

$$c'(nL_+) = (c_{n+1} - c_n \cosh(\beta)) \frac{\beta}{L \sinh(\beta)}$$

and

$$c'(nL_-) = -(c_{n-1} - c_n \cosh(\beta)) \frac{\beta}{L \sinh(\beta)}.$$

Substituting these results into the jump condition yields the difference equation

$$\frac{k_s}{\beta \sinh(\beta)} (c_{n+1} - 2c_n \cosh(\beta) + c_{n-1}) + f(c_n) = 0. \tag{4.20}$$

It is usually not possible to obtain an explicit solution of a nonlinear difference equation. One exception is if $f(c)$ is piecewise linear,

$$f(c) = f_0 H(c - c^*), \tag{4.21}$$

where c^* is a release threshold. Without loss of generality, suppose that the standing wave solution crosses threshold from below in the interval $0 < x < L$. Try a solution of the form $c_n = A_- \mu^{-n}$ for $n \le 0$ and $c_n = C - A_+ \mu^n$ for $n \ge 0$ with $0 < \mu < 1$. The constant C is determined by taking the limit $n \to \infty$ in (4.20) with $c_n \to C > c^*$:

$$\frac{k_s}{\beta \sinh(\beta)}(C - 2C\cosh(\beta) + C) + f_0 = 0,$$

so that

$$C = \frac{\beta \sinh(\beta)}{2\cosh(\beta) - 2}\frac{f_0}{k_c} = \frac{\beta \cosh(\beta/2)}{2\sinh(\beta/2)}\frac{f_0}{k_c}.$$

The constant μ then satisfies the quadratic equation $\mu - 2\lambda + \mu^{-1} = 0$ with $\lambda = \cosh(\beta)$. Choosing the root that is less than one, we have $\mu = \lambda - \sqrt{\lambda^2 - 1} = \mathrm{e}^{-\beta}$. Finally, the factors $A_\pm$ can be determined by considering the difference equation for $n = 0, 1$, which gives [322]

$$A_-(\beta) = \frac{\mu(\beta)C(\beta)}{1 + \mu(\beta)}, \quad A_+(\beta) = \mathrm{e}^{\beta} A_-(\beta).$$

Given that $C, A_\pm$ and $\mu_\pm$ are all functions of β (assuming that f_0/k_c is fixed), the conditions for the existence of a standing wave-front solution are

$$A_-(\beta) < c^*, \quad C(\beta) - A_+(\beta)\mu(\beta) = \mathrm{e}^{\beta} A_-(\beta) \geq c^*. \tag{4.22}$$

For a given β, a traveling wave exists if the threshold c^* lies beneath the curve $A_-(\beta)$, whereas a standing wave exists if c^* lies between $A_-(\beta)$ and $\mathrm{e}^{\beta} A_-(\beta)$; in the latter case propagation failure occurs. Note, in particular, that increasing the threshold c^* or increasing β makes propagation failure more likely. Moreover, increasing β corresponds to increasing the cluster spacing L or decreasing the Ca^{2+} diffusion coefficient D_c.

Having established that wave propagation failure can occur, we now describe how to calculate the wave speed as a function of "discreteness" using the averaging method of Keener [318, 319]. The analysis proceeds along identical lines to the study of inhomogeneous diffusivity in the discrete bistable equation; see Sect. 2.5. First, rewrite (4.17) in the dimensionless form

$$\frac{\partial c}{\partial t} = -c + \frac{\partial^2 c}{\partial x^2} + (1 + g'(x/\varepsilon))f(c), \tag{4.23}$$

where $\varepsilon = \sqrt{L^2 k_c / D} \ll 1$, a factor of k_c^{-1} has been absorbed into f, and $g(x)$ is the periodic sawtooth function, $g(x) = 1/2 - x$ for $0 < x < 1$ and $g(x+n) = g(x)$. (More precisely, $g(x)$ is assumed to be the sum of Gaussians (2.69) of width σ, with the limit $\sigma \to 0$ taken at the end of the calculation.) Suppose that the nonlinear function $f(c)$ is one for which there exists a traveling front solution $c(x,t) = C(x - vt)$ of the homogeneous equation ($g \equiv 0$). The main result of the averaging method is that for ε sufficiently small, there exists a wavelike solution or pulsating wave of the form [318]

$$c(x,t) = C(x - \phi(t)) + \mathcal{O}(\varepsilon), \tag{4.24}$$

where the phase $\phi(t)$ evolves according to [see also (2.72)]

$$\frac{d\phi}{dt} = v - \Phi(\phi/\varepsilon) \tag{4.25}$$

with

$$\Phi(\phi/\varepsilon) = \frac{1}{\Lambda}\int_{-\infty}^{\infty} g'([\xi+\phi]/\varepsilon) f(C(\xi)) C'(\xi) \mathrm{e}^{\nu\xi} d\xi, \tag{4.26}$$

and

$$\Lambda = \int_{-\infty}^{\infty} \mathrm{e}^{\nu\xi} C'(\xi)^2 d\xi. \tag{4.27}$$

Equation (4.25) implies that the solution is not translationally invariant, rather it moves with a time-dependent velocity ϕ'. If $v - \Phi(\phi/\varepsilon)$ is strictly positive then $\phi'(t)$ is a positive, periodic function of t with period

$$T = \int_0^{\varepsilon} \frac{d\phi}{v - \Phi(\phi/\varepsilon)}. \tag{4.28}$$

The mean speed of the wave is $\bar{v} = \varepsilon/T$. On the other hand. if $v - \Phi(\phi/\varepsilon)$ vanishes for some ϕ, then propagation failure is expected to occur.

Averaging method for discrete Ca^{2+} release sites. The first step is to rewrite (4.23) as the first-order system

$$c_x = u, \quad u_x = c_t - (1 + g'(x/\varepsilon)) f(c) + c. \tag{4.29}$$

Introducing the exact change of variables $u = w - \varepsilon g(x/\varepsilon) f(u)$ yields the new system

$$c_x = w - \varepsilon g(x/\varepsilon) f(c), \quad w_x = c_t - f(c) + c + \varepsilon g(x/\varepsilon) f'(c) c_x. \tag{4.30}$$

It can be seen that if the $\mathcal{O}(1)$ system of equations is independent of x/ε, then the lowest-order averaged system reduces to the homogeneous equation, which we are assuming supports a traveling front solution $C(x - vt)$. Including the inhomogeneous factors $g(x/\varepsilon)$ means that the system is no longer translationally invariant. However, we can look for solutions that are close to a traveling front by going to a traveling coordinate system with $\xi = x - \phi(t)$ to give [318]

$$c_\xi - w = -\varepsilon g([\xi+\phi]/\varepsilon) f(c) \tag{4.31a}$$

$$-c_t + w_\xi + \phi' c_\xi + f(c) - c = \varepsilon g([\xi+\phi]/\varepsilon) f'(c) c_\xi. \tag{4.31b}$$

We now seek a perturbative solution of the form

$$c = C(\xi) + \varepsilon c_1(\xi,t) + \ldots, \quad w(\xi) = C'(\xi) + \varepsilon w_1(\xi,t) + \ldots, \quad \phi'(t) = v + \varepsilon \phi_1'(t) + \ldots$$

Substituting into equations (4.31) and collecting terms of equal powers in ε yields a hierarchy of equations, the first of which is

$$\partial_\xi c_1 - w_1 = -g([\xi+\phi]/\varepsilon) f(C) \tag{4.32a}$$

$$-\partial_t c_1 + \partial_\xi w_1 + v w_1 + f'(C) c_1 - c_1 = v g([\xi+\phi]/\varepsilon) f(C) - \phi_1'(t) C' + g([\xi+\phi]/\varepsilon) f'(C) C'. \tag{4.32b}$$

Equations (4.32) can be rewritten as

$$-\begin{pmatrix} 0 \\ \partial_t c_1 \end{pmatrix} + \mathbb{L}\begin{pmatrix} c_1 \\ w_1 \end{pmatrix} = \begin{pmatrix} h_c \\ -\phi_1' C' + h_w \end{pmatrix}, \quad \mathbb{L} = \begin{pmatrix} \partial_\xi & -1 \\ f'(C) - c & \partial_\xi + c \end{pmatrix}, \tag{4.33}$$

with h_c and h_w determined by inhomogeneous terms on the right-hand side of equations (4.32a) and (4.32b), respectively. Following our analysis of the linear operator (2.62), we know that the matrix operator appearing in equation (4.33) has a null space spanned by (C', C''). Similarly, the adjoint operator

$$\mathbb{L}^\dagger = \begin{pmatrix} -\partial_\xi & f'(C)-C \\ -1 & -\partial_\xi + c \end{pmatrix}$$

has the null vector $e^{c\xi}(-C'', C')$. Hence, applying the Fredholm alternative, it follows that $\phi'(t)$ must satisfy the phase equation (4.25) with $\phi(t) = v + \varepsilon\phi_1(t)$.

For the particular choice $f(c) = H(c - c^*)$ used in the analysis of standing waves with $f_0/k_c = 1$, the homogeneous equation is identical to the one analyzed at the end of Sect. 2.2. Thus, there exists a unique traveling front solution of the form (2.23) with corresponding wave speed (2.24). The mean wave speed can then be calculated explicitly along similar lines to Sect. 2.5, so that

$$\bar{v} = \frac{\varepsilon}{2} \frac{1}{\ln\left(\frac{v+\varepsilon/\chi}{v-\varepsilon/\chi}\right)}. \tag{4.34}$$

with $v = (1-2c^*)/\sqrt{c^* - c^{*2}}$ and $\chi = 4[c^* - c^{*2}]$. This would predict propagation failure when $\varepsilon \geq \chi v$, that is,

$$\varepsilon \geq 4(1-2c^*)(\sqrt{c^* - c^{*2}}). \tag{4.35}$$

Since the analysis is based on the assumption that ε is small, we expect this condition to be reasonable when $c^* \approx 0.5$. Taylor expanding about this point the condition for propagation failure is approximately $\varepsilon > 2(1-2c^*)$. Similarly, the condition (4.22) based on the standing wave analysis predicts propagation failure when $\varepsilon/(2(e^\varepsilon - 1)) < c^*$, which reduces to $\varepsilon > 2(1-2c^*)$ when $c^* \approx 1/2$. Thus the two approaches agree for small ε and yield qualitatively similar results for large ε. Finally, as in the analysis of myelinated axons, a cubic nonlinearity for the release function $f(c)$ yields an expression for the mean wave speed that involves exponentially small terms so it is necessary to include higher-order terms in the perturbation analysis in order to obtain sufficient accuracy [318].

4.3.2 The Fire–Diffuse–Fire Model of Ca^{2+} Release

An alternative approach to studying the effects of discrete Ca^{2+} release sites is to consider the so-called *FDF* model [127, 137, 140, 325, 497, 511]. The basic idea of the model is that once the Ca^{2+} concentration reaches a threshold value c^* at a given release site, that site fires and instantaneously releases a fixed amount σ of Ca^{2+} into the cytoplasm [325, 497, 511]. It is also straightforward to take into account the effects of ion pumps by including a decay term and replacing instantaneous release by a fixed pulse of finite width [127]. The FDF model is then almost identical to the SDS model of Ca^{2+} spikes propagating along spiny dendrites [129, 130]. Since the latter model was analyzed in detail in Sect. 3.1, we can carry over the previous results after minor modifications. Therefore, consider the following version of the FDF model [127]:

$$\frac{\partial c}{\partial t} = -\frac{c}{\tau_c} + D_c \frac{\partial^2 c}{\partial x^2} + \sum_n \delta(x - x_n)\eta(t - T_n), \tag{4.36}$$

where T_n is the firing time of the site x_n, which only fires once:

$$T_n = \inf\{t \,|\, c(x_n, t) \geq c^*\}. \tag{4.37}$$

For concreteness, let

$$\eta(t) = (\sigma/\tau_d)H(t)H(\tau_d - t),$$

so that each Ca^{2+} puff or spark is of size σ and duration τ_d. Suppose that the Ca^{2+} release sites are regularly spaced, $x_m = mL$, and consider a saltatory wave solution $T_m = m\Delta$ with speed $v = L/\Delta$. The existence of such a wave can be determined straightforwardly by noting that (4.36) is identical to (3.33) under the mapping

$$V \to c, \quad \frac{\bar{n}}{r_s}\eta_0 \to \frac{\sigma}{\tau_d}.$$

The one major difference between the two models is that thresholding in the SDS model is mediated by an IF process (3.2), which introduces an additional time constant $\hat{\tau}$. Therefore, in order to apply the analysis of saltatory waves along a spiny dendrite to the FDF model (see in Sect. 3.1.3), we need to take the limit $\hat{\tau} \to 0$. This then gives the following threshold condition for the existence of a saltatory wave:

$$c^* = \sum_{n=1}^{\infty} H(nL, n\Delta), \tag{4.38}$$

with

$$H(x,t) = \frac{\sigma}{\tau_d}\int_0^{\tau_d} G_0(x, t-s)\mathrm{d}s, \quad G_0(x,t) = \frac{1}{\sqrt{4\pi D_c t}}\mathrm{e}^{-t/\tau_c - x^2/4D_c t}. \tag{4.39}$$

In the limit $\tau_d \to 0$, $H(x,t) \to \sigma G_0(x,t)$ and the threshold condition becomes

$$\begin{aligned} c^* &= \sigma \sum_{n=1}^{\infty} G_0(nL, n\Delta) \\ &= \sigma \sum_{n=1}^{\infty} \frac{1}{\sqrt{4\pi D_c n\Delta}} \exp\left(-n\left[\frac{L^2 t}{4D_c\Delta} + \frac{\Delta}{\tau_c}\right]\right) \equiv g(\Delta). \end{aligned} \tag{4.40}$$

In the additional limit $\tau_c \to \infty$ (i.e., neglecting the flux due to ion pumps), the results of [497] are recovered. In particular, $g(\Delta)$ becomes a monotone function of Δ, and the speed of the traveling waves scales linearly as D_c/L. The latter follows after introducing the dimensionless threshold $\tilde{c}^* = c^* L/\sigma$ and noting that Lg/σ is then only a function of the dimensionless quantity $\Delta D_c/L^2$. However, this result is inconsistent with the analysis of standing waves, which showed that propagation failure can occur by decreasing the diffusion coefficient. The discrepancy is resolved by taking into account the effects of ion pumps, that is, taking τ_c to be finite. Moreover, $g(\Delta)$

is now non-monotone and consequently one finds two solution branches with the faster one corresponding to stable waves [127]. This result also holds in the case of finite pulse width τ_d, for which

$$H(x,t) = \frac{\sigma}{\tau_d}\left[A(x,t-\min(t,\tau_d)) - A(x,t)\right], \tag{4.41}$$

with $A(x,t)$ given by (3.40). In summary, the main qualitative results of the SDS model carry over to the FDF model, for example, one finds that propagation failure occurs if the spacing between release sites becomes too large.

One of the limitations of the above FDF model is that it neglects variations in the Ca^{2+} concentration within the ER. However, in many cells, Ca^{2+} release can result in a significant local depletion of ER Ca^{2+}. In order to take this into account, the FDF model has been extended in the form of a bidomain threshold-release model [621, 622]:

$$\frac{\partial c}{\partial t} = D_c \frac{\partial^2 c}{\partial x^2} + J_{rel}(c,c_e) - J_2(c,c_e) \tag{4.42a}$$

$$\frac{\partial c_e}{\partial t} = D_e \frac{\partial^2 c}{\partial x^2} - \chi_e\left[J_{IP}(c,c_e) - J_2(c,c_e)\right], \tag{4.42b}$$

where the release and uptake fluxes, $J_{rel}(c,c_e) - J_2(c,c_e)$, are functions of the cytosolic and ER Ca^{2+} concentrations. For simplicity, assume that there is a continuous and uniform distribution of Ca^{2+} release sites and that the release flux depends on the difference in the cytosolic and ER Ca^{2+} concentrations:

$$J_{rel}(x,t) \equiv J_{rel}(c(x,t),c_e(x,t)) = (c_e(x,t) - c(x,t))\eta(t - T(x)), \tag{4.43}$$

with

$$T(x) = \inf\{t \,|\, c(x,t) \geq c^*\}. \tag{4.44}$$

The release sites could be either RyRs or IP_3Rs; in the latter case the IP_3 concentration p is held fixed. Finally, the reuptake flux due to the action of ion pumps is taken to have the linear form

$$J_2(c,c_e) = \frac{c}{\tau_c} - \frac{c_e}{\tau_e}. \tag{4.45}$$

The existence and stability of a solitary pulse solution of (4.42) can be investigated along similar lines to Sect. 3.1.1.

4.4 Stochastic Models of Ca^{2+} Release

The fluorescent imaging of localized Ca^{2+} puffs and sparks has established that Ca^{2+} release is a stochastic process that occurs at spatially discrete sites consisting of clusters of IP_3Rs and RyRs, respectively. In *Xenopus* oocytes, Ca^{2+} puffs have an amplitude ranging from around 50 to 600 nM, a spatial spread of approximately

6 μm and a typical duration of 1 s [489, 490, 690]. For sufficiently high levels of IP_3 concentration, the amplification of Ca^{2+} puffs by CICR can lead to the formation of Ca^{2+} waves. Ca^{2+} sparks in heart and skeletal muscle tend to be of shorter duration and less spatial spread and are less likely to result in wave propagation [110, 111]. As we have already mentioned Ca^{2+} puffs and sparks have also been observed in neurons [534], suggesting that one needs to take into account stochastic release events when modeling Ca^{2+} waves. Typically, one combines a stochastic model of localized release through RyRs or IP_3Rs with a deterministic reaction–diffusion model of Ca^{2+} waves such as the FDF model [137, 320]. The stochastic modeling of the Ca^{2+}-dependent opening and closing of these receptors proceeds along analogous lines to the modeling of voltage-gated ion channels considered in Sect. 1.5.

4.4.1 Stochastic Model of Ca^{2+} Puffs in a Cluster of IP_3Rs

Stochastic models of Ca^{2+} puffs typically treat a cluster of IP_3Rs as a set of N channels that open and close independently, but are indirectly coupled by the common cytoplasmic Ca^{2+} concentration [180, 182, 579, 612]. Models differ in the level of detail regarding individual receptors. The first deterministic kinetic model of Ca^{2+}-gated IP_3Rs was proposed by De Young and Keizer, in their study of agonist-induced Ca^{2+} oscillations. This model assumes that the IP_3 receptor consists of three equivalent receptor subunits, all of which have to be in a conducting state in order to generate a Ca^{2+} flux. Each subunit is taken to have an IP_3-binding site, an activating Ca^{2+}-binding site, and an inactivating Ca^{2+}-binding site; the conducting state corresponds to the state in which all subunits have the first two binding sites occupied but the third unoccupied. Although the De Young–Keizer model is simple to describe, it involves a relatively large number of variables that have to be coupled to the Ca^{2+} and IP_3 concentrations. A simplified version of the model was subsequently developed by Li and Rinzel [381]. They exploited the fact that the binding of IP_3 and activating Ca^{2+} are fast relative to inactivating Ca^{2+} and used a quasi-steady-state argument to reduce the eight-state subunit model to a model that simply keeps track of whether or not the inactivating Ca^{2+}-binding site of a subunit is occupied. More specifically, the Li–Rinzel model is a two-variable model given by

$$\frac{dc}{dt} = J_{\mathrm{IP}} + J_{\mathrm{leak}} - J_{\mathrm{p2}} \tag{4.46a}$$

$$\frac{dh}{dt} = \alpha_h(1-h) - \beta_h h, \tag{4.46b}$$

where c is the cytoplasmic Ca^{2+} concentration, h is the fraction of receptors in a cluster not inactivated by Ca^{2+}, and p is the IP_3 concentration, which is assumed fixed. The three Ca^{2+} fluxes included in the model are the channel flux J_{IP} and

leakage flux $J_{\rm leak}$ from the ER to the cytoplasm, and the flux $J_{\rm p2}$ pumped back into the ER; see also Fig. 4.2. The expressions for the various fluxes are

$$J_{\rm IP} = f(c,p)h^3[c_e - c], \quad J_{\rm leak} = \nu_0[c_e - c], \quad J_{\rm P2} = \frac{\nu_1 c^2}{k_3^2 + c^2}, \tag{4.47}$$

with

$$f(c,p) = \left(\frac{p}{p+k_4}\right)^3 \cdot \left(\frac{c}{c+k_5}\right)^3, \quad \alpha_h = \nu_2 \frac{p+k_4}{p+k_6}, \quad \beta_h = \nu_3 c. \tag{4.48}$$

The various cubic terms reflect the existence of three subunits. Parameter values of the model can be found in [381]. We see that the simplified model resembles the Hodgkin–Huxley model (see Sect. 1.1), after replacing Ca^{2+} concentration c by membrane voltage v and c_e by a reversal potential.

We now describe a stochastic version of the Li–Rinzel model for a cluster of IP_3Rs due to Shuai and Jung [579]. For stochastic versions of the full De Young–Keizer model, see, for example, [180, 182, 244, 612]. The deterministic equations (4.46) describe the mean behavior of a large cluster of Ca^{2+} channels, just as the Hodgkin–Huxley equations for membrane voltage apply to a large number of voltage-gated ion channels. As we discussed in Sect. 1.5, if the number of channels is relatively small, then it is necessary to take into account thermally driven fluctuations in the opening and closing of individual channels. In the case of the Li–Rinzel model, one only needs to consider the opening and closing process for the gating variable h of each subunit. The latter is modeled as the two-state Markov process

$$C(\text{closed}) \underset{\beta_h(c)}{\overset{\alpha_h}{\rightleftharpoons}} O(\text{open}). \tag{4.49}$$

Suppose that there are N independent IP_3Rs, each with three independent subunits labeled $i = 1,2,3$ that are described by the above two-state Markov process. Let $N_i(t)$ $(i = 1,2,3)$ denote the number of receptors at time t that have the ith subunit open. Under the adiabatic assumption that the Ca^{2+} concentration c evolves much more slowly than the state transitions of the channels, we can write down a master equation for the probability $P(n_i,t) = \text{Prob}[N_i(t) = n_i | N_i(0) = n_0]$ according to

$$\begin{aligned} \frac{dP(n_i,t)}{dt} &= (N - n_i + 1)\alpha_h P(n_i - 1,t) + (n_i + 1)\beta_h P(n_i + 1,t) \\ &\quad - (n_i\beta_h + (N - n_i)\alpha_h)P(n_i,t), \quad i = 1,2,3. \end{aligned} \tag{4.50}$$

As with voltage-gated ion channels, we have a stochastic hybrid system, since the transition rate β_h depends on the Ca^{2+} concentration $c(t)$, which evolves according to a piecewise deterministic equation of the form (4.46a). The latter, in turn, couples to the discrete stochastic variables $N_i(t)$ through the flux

$$J_{\rm IP} = f(c(t),p)[c_e - c(t)] \prod_{i=1}^{3} \frac{N_i(t)}{N}. \tag{4.51}$$

[Note that one should really write down a differential Chapman–Kolmogorov equation for the joint probability density $p(n_1,n_2,n_3,c,t)$ along the lines of (1.126)]. Finally, for large N, one can obtain a further simplification by carrying out a Kramers–Moyal expansion of the master equation (4.50) along the lines of Sect. 1.5.2. This yields the following SDE for $H_i(t) = N_i(t)/N$ with H_i treated as a continuous stochastic variable:

$$dH_i = \alpha_h(1-H_i) - \beta_h H_i + \frac{1}{\sqrt{N}} b(H_i) dW_i, \tag{4.52}$$

where

$$b(H_i) = \sqrt{\alpha_h(1-H_i) + \beta_h H_i},$$

and $W_i(t)$ is an independent Wiener process with

$$\langle dW_i(t) \rangle = 0, \quad \langle dW_i(t) dW_j(t') \rangle = \delta(t-t') dt\, dt' \delta_{i,j}.$$

Shuai and Jung [579] simulated the stochastic Li–Rinzel model in order to investigate the effects of noise on Ca^{2+} oscillations in a space-clamped model. They assumed that the deterministic system (4.46) was monostable at low and high IP_3 concentrations and exhibited limit cycle oscillations (occurring via a Hopf bifurcation) at intermediate concentrations. They showed that noise can enlarge the range of IP_3 concentrations over which oscillations occur—an effect known as *coherence resonance*. They also found a broad distribution of puff amplitudes, lifetimes, and interpuff intervals. In particular, at low IP_3 concentrations, the amplitude distribution is a monotonically decaying function, whereas at higher concentrations, it is unimodal. This suggests that Ca^{2+} puffs become more significant as IP_3 concentration is increased and hence could impact the spontaneous generation of Ca^{2+} waves. This issue was investigated numerically by Falcke [180] using a stochastic version of the De Young–Keizer model that was incorporated into a reaction–diffusion model of spatially distributed channel clusters. He showed that there is indeed a transition from Ca^{2+} puffs to waves as the IP_3 concentration is increased. At low concentrations, only puffs occur, since there is not enough Ca^{2+} released to stimulate neighboring clusters, which means that the response is purely local. However, as IP_3 concentration increases, global Ca^{2+} waves can emerge from local nucleation sites of high Ca^{2+} concentration. At intermediate levels of IP_3, global events are rare and waves only progress a short distance before dying out. On the other hand, for higher IP_3 concentrations, global waves occur regularly with a well-defined period. Again this oscillatory-like behavior can occur in parameter regimes for which the deterministic model is non-oscillatory.

4.4.2 Stochastic Model of Ca^{2+} Sparks in a Cluster of RyRs

We now turn to a stochastic model of Ca^{2+} sparks due to Hinch [276]; see also [241]. This model was originally developed for *cardiac myocytes* (heart muscle cells) and

includes details of the geometry of Ca^{2+} release units, in particular, the narrow junctional gap known as the diadic space that separates the sarcoplasmic reticulum (SR) from the plasma membrane; see Fig. 4.4. (In smooth muscle cells the smooth ER is referred to as the sarcoplasmic reticulum.) However, it is possible that a similar mechanism occurs in neurons at the specialized subsurface cisternae of the ER, which also form narrow junctions with the plasma membrane; see Fig. 4.2. In a typical myocyte, there could be up to 10,000 Ca^{2+} release units, each one containing a cluster of around $N = 50$ RyRs on the surface of the SR. The cluster of RyRs is apposed to L-type Ca^{2+} channels located on so-called t-tubules, which are invaginations of the plasma membrane into the myocyte. (The Ca^{2+} channels are not involved in the spontaneous generation of Ca^{2+} sparks so are ignored in the model.) The diadic space separating the SR from the t-tubules is a region of the mytoplasm (intracellular fluid of myocytes), which is approximately cylindrical in shape with width 10 nm and radius 100 nm. Since the diadic space is a small enclosed volume, it supports an elevation in Ca^{2+} concentration relative to the bulk mytoplasm following the release of Ca^{2+} from an RyR. Such a local elevation plays a crucial role in the Ca^{2+}-induced Ca^{2+}-release (CICR) that results in a Ca^{2+} spark. The SR in a neighborhood of the RyRs is known as the junctional SR (JSR), which may have a different Ca^{2+} concentration from the bulk or network SR (NSR).

We now briefly introduce the model of Hinch in nondimensional form; details of model approximations and estimates of experimentally based model parameters can be found in [276]. First, the diadic space is modeled as a single compartment with Ca^{2+} concentration c satisfying the current conservation equation

$$\tau_D \frac{dc}{dt} = J_{\mathrm{RyR}} - J_{\mathrm{D}}. \tag{4.53}$$

Here τ_D is a time constant, J_{RyR} is the total Ca^{2+} current through the RyRs, and J_{D} is the diffusive current from the diadic space to the bulk mytoplasm. The latter is modeled as the Fickian current

$$J_{\mathrm{D}} = c - c_m, \tag{4.54}$$

where c_m is the bulk mytoplasm Ca^{2+} concentration. The total current through the RyRs is taken to be proportional to the number n of open RyRs times the Ca^{2+} concentration c_{sr} in the JSR:

$$J_{\mathrm{RyR}} = c_{\mathrm{sr}} x, \quad x = \frac{n}{N}, \tag{4.55}$$

with N the total number of RyRs in the cluster. Each RyR has Ca^{2+}-binding sites, which can be activating or deactivating. When an RyR is in an activated state it is promoted to a mode where it continuously opens and closes according to a Markov process (see Sect. 1.5), with a mean open time of 1 ms [695]. The opening of an RyR channel results in an extra Ca^{2+} current flowing into the diadic space, which increases the rate at which Ca^{2+} binds to the other RyRs via CICR, thus creating a positive feedback loop. This feedback loop provides a mechanism for bistability.

Note that the RyRs also contain inactivating Ca^{2+}-binding sites, but these do not play a role in initiating a Ca^{2+} spark so are not included in the model. For simplicity, the RyRs are modeled using a two-state Markov process involving a single closed state and a single open state (see also [324]):

$$C(\text{closed}) \underset{k_-}{\overset{k_+(c)}{\rightleftharpoons}} O(\text{open}), \tag{4.56}$$

with transition rates

$$k_+(c) = \frac{1}{k\tau_o}\frac{c^\alpha}{c^\alpha + 1}, \quad k_- = \frac{1}{\tau_o}. \tag{4.57}$$

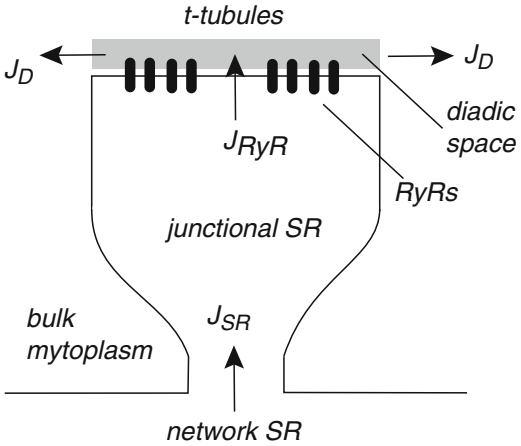

Fig. 4.4 Schematic diagram of a Ca^{2+} release unit in a cardiac myocyte. It is divided into four compartments: the network SR, the junctional SR, the diadic space, and the bulk mytoplasm. See text for details

Here τ_o is the mean open time of an RyR, α is the number of Ca^{2+} ions that are needed to open an RyR, and k determines the proportion of time the RyRs are open. It is assumed that the RyRs are gated independently of each other. They are, however, indirectly coupled via the Ca^{2+} concentration in the diadic space. The time constant τ_D of diffusive flux from the diadic space is several orders of magnitude smaller than the mean open time τ_o of an RyR, that is, $\tau_D \sim 3\,\mu s$ whereas $\tau_o \sim 1\,ms$. Therefore, the Ca^{2+} concentration in the diadic space can be taken to be in quasi-equilibrium, $\tau_D \to 0$, so that

$$c = c_m + c_{sr}x. \tag{4.58}$$

It follows that the transition rate can be reexpressed as a function of the fraction of open channels and the Ca^{2+} concentration in the SR, $k_+ = k_+(c_m + c_{sr}x)$.

Now consider N independent RyRs within a Ca^{2+} release unit, each described by the above two-state Markov process. Let $N(t)$ be the number of open channels at

time t and set $p_n(t) = \text{Prob}[N(t) = n|N(0) = n_0]$. Following along similar lines to Sect. 1.5.1, it can be shown that $p_n(t)$ evolves according to a master equation with transitions rates $\omega_\pm(n/N) : n \to n \pm 1$:

$$\omega_+(x) = N(1-x)\frac{(c_m + c_{\rm sr}x)^\alpha}{k((c_m + c_{\rm sr}x)^\alpha + 1)}, \quad \omega_-(x) = Nx. \tag{4.59}$$

For the moment, it is assumed that c_m and $c_{\rm sr}$ are fixed so that ω_+ can be treated as a function of x alone. (In Sect. 4.4.4, the dynamics of c_{sr} following initiation of a Ca^{2+} spark will also be taken into account.) The units of time are fixed by setting $\tau_{\rm o} = 1$. The master equation for the RyR cluster is then

$$\frac{dp_n}{dt} = \omega_+((n-1)/N)p_{n-1} + \omega_-((n+1)/N)p_{n+1} - (\omega_+(n/N) + \omega_-(n/N))p_n, \tag{4.60}$$

with boundary conditions $p_{N+1} = p_{-1} \equiv 0$. Multiplying both sides of the master equation (4.60) by n/N and summing over n gives

$$\frac{d\langle n/N\rangle}{dt} = \langle \Omega_+(n/N)\rangle - \langle \Omega_-(n/N)\rangle, \tag{4.61}$$

where $\omega_\pm = N\Omega_\pm$, and the brackets $\langle \ldots \rangle$ denote a time-dependent ensemble averaging over realizations of the stochastic dynamics, that is, $\langle A(n/N)\rangle = \sum_n p_n A(n/N)$ for any function of state $A(n/N)$. In the thermodynamic limit $N \to \infty$ (infinite cluster size), statistical correlations can be ignored so that one can take the mean-field limit $\langle \Omega_\pm(n/N)\rangle \to \Omega_\pm(\langle n/N\rangle)$. This then yields a deterministic equation for the fraction x of open RyRs:

$$\frac{dx}{dt} = \Omega_+(x) - \Omega_-(x) = (1-x)\frac{(c_m + c_{\rm sr}x)^\alpha}{k((c_m + c_{\rm sr}x)^\alpha + 1)} - x. \tag{4.62}$$

It can be shown that, for physiologically reasonable parameter values, this equation exhibits bistability [276], that is, there exists a pair of stable fixed points $x_\pm$ separated by an unstable fixed point x_0. The fixed point $x_- \approx 0$ represents a quiescent state, whereas the other fixed point x_+ represents a Ca^{2+} spark in which a significant fraction of RyRs are in the active mode and can be interpreted as a burst phase. Hence, this model operates in a completely different regime to the model considered by Shuai and Jung [579], which was in a monostable state (a fixed point or limit cycle) in the deterministic limit. Bistability of the Hinch model means that a Ca^{2+} spark is a distinct event rather than a broad distribution of events.

Noise-induced transitions from x_- to x_+ determine the distribution of inter-spark intervals, just as noise-induced transitions from x_+ to x_- determine the distribution of spark lifetimes. Hence, estimating the mean time for the occurrence of a spark event reduces to the problem of calculating the MFPT to reach x_+, starting from a neighborhood of x_-, by crossing x_0. (The dominant contribution to this MFPT is the time to reach x_0, since the system then quickly relaxes to x_+.) We encountered an analogous problem in Sect. 1.5, where we considered the mean time

for spontaneous action potential initiation due to ion-channel fluctuations. We first estimated the MFPT by carrying out a diffusion approximation of the underlying master equation (1.104), and calculating the MFPT of the corresponding Fokker–Planck equation. However, the diffusion approximation resulted in exponentially large errors. Therefore, we considered an alternative approach in Sect. 1.6, which was based on WKB methods and asymptotic analysis. Here we consider a corresponding WKB approximation of the master equation (4.60). Such an approach has been used increasingly to analyze escape problems in chemical and biological systems [160, 164, 175, 176, 256, 339, 340], including the Ca^{2+} release model of Hinch [277]. Note, however, that in contrast to the analysis of membrane voltage fluctuations in Sect. 1.6, the analysis of calcium sparks is performed with respect to the small parameter $1/N$ rather than ε. That is, we carry out a system-size expansion rather than assuming fast kinetics. For the moment, we simply state the results and leave the details to Sect. 4.4.3.

If x_- is not on the boundary $x = 0$ then a standard analysis shows that the mean time τ_i to initiate a Ca^{2+} spark starting from the quiescent state x_- is

$$\tau_i = \frac{2\pi}{\Omega_+(x_-)\sqrt{|\gamma(x_0)|\gamma(x_-)}} e^{N[\Phi(x_0)-\Phi(x_-)]}. \tag{4.63}$$

with

$$\gamma(x) = \frac{\Omega_-'(x)}{\Omega_-(x)} - \frac{\Omega_+'(x)}{\Omega_+(x)}, \quad \Phi(x) = \int^x \ln\left(\frac{\Omega_-(y)}{\Omega_+(y)}\right) dy.$$

Similarly, the mean duration τ_f of a spark, which corresponds to the mean time to transition back from x_+ to x_-, is given by

$$\tau_f = \frac{2\pi}{\Omega_+(x_+)\sqrt{|\gamma(x_0)|\gamma(x_+)}} e^{N[\Phi(x_0)-\Phi(x_+)]}. \tag{4.64}$$

Note that at a fixed point x_j, $\Omega_+(x_j) = \Omega_-(x_j)$ so that $\text{sign}(\gamma(x_j)) = \text{sign}(\Omega_-'(x_j) - \Omega_+'(x_j))$. Thus, $\gamma(x_0) < 0$ (unstable) and $\gamma(x_\pm) > 0$ (stable). One also finds that $\Phi(x_0) > \Phi(x_\pm)$ so that τ_i, τ_f are exponentially large. It turns out that in the case of Ca^{2+} release, the quiescent state x_- is in an $\mathcal{O}(1/N)$ neighborhood of the boundary $x = 0$, so that the prefactor of the MFPT has to be modified accordingly; see [276, 277] for details. Nevertheless, the leading order exponential is unchanged. From the perspective of modeling stochastic Ca^{2+} waves using the FDF model of Sect. 4.3.2, the main result that emerges from the analysis of Ca^{2+} sparks is that the deterministic threshold mechanism needs to be replaced by a probabilistic mechanism. In the deterministic case, a cluster of receptors fires whenever the intracellular Ca^{2+} crosses a fixed threshold. On the other hand, in a stochastic FDF model, Ca^{2+} release is a probabilistic process. Given the MFPT τ_i, the probability of a spark event in a time interval t is given by

$$P_i(t) = 1 - e^{-t/\tau_i}. \tag{4.65}$$

Recall that the transition rates $\Omega_\pm$, and thus τ_i, are functions of the Ca^{2+} concentration c_m of the mytoplasm, which has so far been assumed fixed. Indeed, one finds that the probability of release in a given time interval t is a sigmoidal function of c_m [276]. This stochastic release process can now be incorporated into a stochastic version of the FDF model by taking the sequence of release times T_n in (4.36) to be generated according to a sigmoidal probability distribution that is parameterized by the Ca^{2+} concentration in the mytoplasm, which itself evolves according to (4.36); see [137, 320] for details. The resulting model can be used to simulate the spontaneous occurrence of Ca^{2+} waves.

4.4.3 WKB Method and Quasistationary Approximation

We now present the details of how to calculate the rate of escape from a metastable state. Although, we focus here on the particular problem of Ca^{2+} release, the basic approach applies to the master equation of any bistable system in the large N (weak noise) limit. Throughout the analysis we will switch between n/N and x, with x treated as a continuous variable; this is a reasonable approximation when N is large. First, note that the master equation (4.60) with the given reflecting boundary conditions at $x = 0, 1$ has a unique stationary state given by (see also Sect. 1.5.1)

$$p_n^* = p_k^* \prod_{m=k+1}^{n} \frac{\Omega_+((m-1)/N)}{\Omega_-(m/N)} = p_k^* \exp\left(\sum_{m=1}^{n} \ln\left(\frac{\Omega_+((m-1)/N)}{\Omega_-(m/N)} \right) \right). \quad (4.66)$$

The functions $\Omega_\pm(x)$ are smooth and the second derivatives of $\ln \Omega_\pm(x)$ are bounded (except in the limits $x \to 0$ and $x \to 1$). Therefore, away from the boundaries, the sums can be approximated by the trapezium rule [276]

$$\sum_{m=k}^{n} \ln(f(m/N)) = \frac{\ln(f(k/N) + \ln f(n/N)}{2} + N \int_{k/N}^{n/N} \ln(f(y)) dy + \mathcal{O}(1/N),$$

so that

$$p_n^* = \frac{\mathcal{N}}{\sqrt{\Omega_+(x)\Omega_-(x)}} e^{-N\Phi(x)}, \quad x = n/N, \quad (4.67)$$

where $\Phi(x)$ is the effective potential

$$\Phi(x) = \int^x \ln\left(\frac{\Omega_-(y)}{\Omega_+(y)} \right) dy, \quad (4.68)$$

and $\mathcal{N}$ is a normalization factor such that $\sum_{n=0}^{N} p_n^* = 1$.

Now suppose that we place an absorbing boundary at the unstable fixed point $x_0 = n_0/N$. Although there no longer exists a stationary solution, the flux through the absorbing boundary is exponentially small for large N, so that we can use a

spectral projection method analogous to Sect. 1.6. First, rewrite the master equation (4.60) for $n = 0, \ldots, n_0$ as the linear system

$$\frac{d\mathbf{p}}{dt} = \mathbf{Q}\mathbf{p}, \tag{4.69}$$

where $\mathbf{p} = (p_0(t), p_1(t), \ldots, p_{n_0}(t))^T$, $\mathbf{Q}$ is the matrix of transition rates, and $p_{n_0}(t) = 0$ (absorbing boundary condition). Suppose that the eigenvalues of $\mathbf{Q}$ are ordered according to $0 > \lambda_0 \geq \mathrm{Re}[\lambda_1] \geq \mathrm{Re}[\lambda_2] \geq \ldots$ with corresponding eigenfunctions $\phi_n^{(j)}$, and consider the eigenfunction expansion

$$p_n(t) = \sum_{r=0}^{n_0} C_r \mathrm{e}^{-\lambda_r t} \phi_n^{(r)}. \tag{4.70}$$

We assume that $|\lambda_0| \sim \mathrm{e}^{-\eta N}$ for $\eta = \mathscr{O}(1)$, whereas λ_r for $r > 0$ are only weakly dependent on N. It follows that all other eigenmodes decay to zero much faster than the perturbed stationary density. Thus at large times, we have the quasistationary approximation

$$p_n(t) \sim C_0 \mathrm{e}^{-\lambda_0 t} \phi_n^{(0)}. \tag{4.71}$$

One can now use a WKB ansatz (see below) to generate a quasistationary solution ϕ_n^ε for which $\mathbf{Q}\phi^\varepsilon = 0$ and $\phi_{n_0}^\varepsilon \sim \mathscr{O}(\mathrm{e}^{-\eta N})$. Since the WKB solution does not satisfy the absorbing boundary condition, it is necessary to perform an asymptotic expansion in order to match the quasistationary solution with the solution in a neighborhood of x_0. In the process this determines λ_0, whose inverse can be identified as the MFPT to escape from the basin of attraction of the metastable state x_-.

Dropping exponentially small terms and writing $\phi_n^\varepsilon = \phi^\varepsilon(x)$ with x treated as a continuous variable, we have

$$\begin{aligned} 0 = {} & \Omega_+(x-1/N)\phi^\varepsilon(x-1/N) \\ & +\Omega_-(x+1/N)\phi^\varepsilon(x+1/N) - (\Omega_+(x)+\Omega_-(x))\phi^\varepsilon(x). \end{aligned} \tag{4.72}$$

We seek a WKB solution of the form

$$\phi^\varepsilon(x) \sim K(x;\varepsilon)\mathrm{e}^{-\Phi(x)/\varepsilon}, \tag{4.73}$$

with $K(x;\varepsilon) \sim \sum_{m=0}^\infty \varepsilon^m K_m(x)$. Substituting (4.73) into (4.72), Taylor expanding with respect to ε, and collecting the $\mathscr{O}(1)$ terms gives

$$\Omega_+(x)(\mathrm{e}^{\Phi'(x)} - 1) + \Omega_-(x)(\mathrm{e}^{-\Phi'(x)} - 1) = 0, \tag{4.74}$$

where $\Phi' = d\Phi/dx$. Solving this quadratic equation in $\mathrm{e}^{\Phi'}$ shows that

$$\Phi = \int^x \ln \frac{\Omega_-(y)}{\Omega_+(y)} dy \quad \text{or} \quad \Phi = \text{constant}. \tag{4.75}$$

Proceeding to the next level, equating terms at $\mathcal{O}(\varepsilon)$ gives

$$\Omega_+ e^{\Phi'}\left(-\frac{K_0'}{K_0}+\frac{\phi''}{2}\right)+\Omega_- e^{-\Phi'}\left(\frac{K_0'}{K_0}+\frac{\phi''}{2}\right)-\Omega_+' e^{\Phi'}+\Omega_- e^{-\Phi'}=0.$$

Substituting for Φ using (4.74) and solving for K_0 yields the following leading order forms for ϕ^ε:

$$\phi^\varepsilon(x)=\frac{A}{\sqrt{\Omega_+(x)\Omega_-(x)}}e^{-N\Phi(x)}. \tag{4.76}$$

with Φ given by (4.75), which is sometimes called the activation solution, and

$$\phi^\varepsilon(x)=\frac{B}{\Omega_+(x)-\Omega_-(x)}, \tag{4.77}$$

which is sometimes called the relaxation solution. The constants A, B are determined by matching solutions around x_0. Clearly, (4.77) is singular at any fixed point x_j, where $\Omega_+(x_j)=\Omega_-(x_j)$, so is not a valid solution for the required quasistationary density. On the other hand, it does have an interpretation in terms of a corresponding Hamiltonian–Jacobi formulation of the WKB ansatz.

The WKB ansatz was also used in the analysis of metastability in stochastic ion-channel models in Sect. 1.6 and in the analysis of sharp interfaces for slowly modulated pulled fronts; see Sect. 3.2.4. Following along similar lines to the latter example, we can formally interpret (4.74) as a stationary Hamilton–Jacobi equation $H(x,\Phi'(x))=0$ for Φ, with Hamiltonian

$$H(x,p)=\sum_{r=\pm}\Omega_r(x)\left[e^{rp}-1\right]. \tag{4.78}$$

This suggests a corresponding classical mechanical interpretation, in which H determines the motion of a particle with position x and conjugate momentum p. A trajectory of the particle is given by the solution of Hamilton's equations

$$\dot{x}=\frac{\partial H}{\partial p}=\sum_{r=\pm1}r\Omega_r(x)e^{rp} \tag{4.79}$$

$$\dot{p}=-\frac{\partial H}{\partial x}=\sum_{r=\pm1}\frac{\partial\Omega_r}{\partial x}(x)\left[e^{rp}-1\right]. \tag{4.80}$$

Here the time t should be viewed as a parameterization of paths rather than as a real time variable. Introducing the Lagrangian

$$L(x,\dot{x})=p\cdot\dot{x}-H(x,p), \tag{4.81}$$

it follows that $\Phi(x)$ with $\Phi(\bar{x})=0$ corresponds to the classical action evaluated along the least-action trajectory from $\bar{x}$ to x:

$$\Phi(x)=\inf_{x(t_0)=\bar{x},x(T)=x}\int_0^T L(x,\dot{x})dt. \tag{4.82}$$

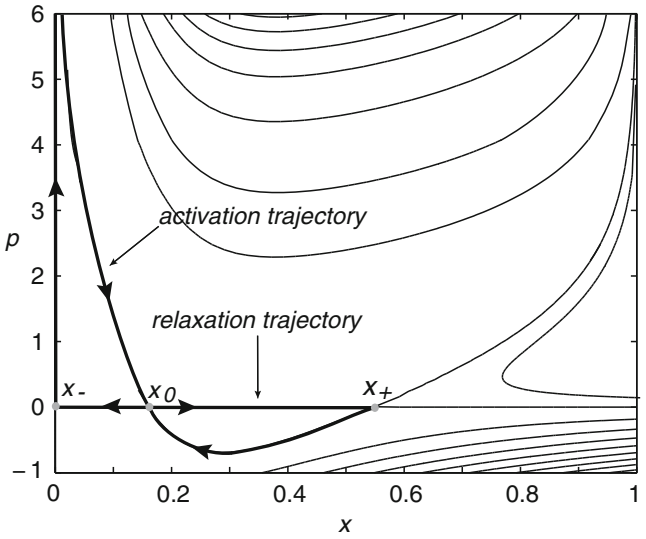

Fig. 4.5 Phase portrait of Hamiltonian equations of motion for $\Omega_\pm = \omega_\pm/N$ given by equation (4.59) with $c_m = 0.01, c_e = 4, \alpha = 4$ and $k = 0.8$. The zero-energy solutions are shown as *thicker curves*

In terms of the underlying stochastic process $X(t)$, the least-action path can be interpreted as the most probable fluctuational path from $\bar{x}$ to x (in the large-N limit) [205, 398]. Since $p = S'$ everywhere along this path, we have

$$\Phi(x) = \int_{\bar{x}}^{x} p(x')dx', \tag{4.83}$$

with the integral taken along the trajectory. It follows that the leading order term in the WKB approximation is determined by finding zero-energy solutions $p = p(x)$ such that $H(x, p(x)) = 0$. One solution is $p = 0$ or $\Phi =$ constant, which represents the classical action along a deterministic (or relaxation) trajectory. For example, once the system escapes from the metastable state x_-, it tends to rapidly converge to the other metastable state x_+ along such a deterministic path. (The contribution of relaxation trajectory to the mean escape time is usually neglected.) Another solution for Φ is (4.75), which can be interpreted as the action along a non-deterministic path that represents the most probable path of escape from x_- to x_0 [160, 164, 175, 176]. In Fig. 4.5 we illustrate the Hamiltonian phase space for the model showing the constant energy solutions of the Hamiltonian given by (4.78); the zero-energy activation and relaxation trajectories through the fixed points of the deterministic system are highlighted as thicker curves

Given the quasistationary approximation, the rate of escape from the metastable state centered about $x = x_-$ can be calculated by matching it with an appropriate inner solution in a neighborhood of the point $x = x_0$ [160, 164, 175, 256, 277]. This is necessary since the quasistationary solution (4.76) does not satisfy the absorbing

boundary condition at the point x_0 separating the two metastable states. There are a number of different ways of carrying out the matched asymptotics; see, for example, [277]. Here we will follow an approach based on fixing the probability flux J_0 through x_0 and then matching the activation solution for $x < x_0$ with the relaxation solution for $x > x_0$ using a diffusion approximation of the full master equation (4.60) in the vicinity of x_0 [164, 175, 256]. The latter yields the Fokker–Planck equation (1.111), which can be rewritten in the form of a conservation equation

$$\frac{\partial}{\partial t}P(x,t) = -\frac{\partial}{\partial x}J(x,t) \tag{4.84}$$

with

$$J(x,t) = (\Omega_+(x) - \Omega_-(x))P(x,t) - \frac{1}{2N}\frac{\partial}{\partial x}\left[(\Omega_+(x) + \Omega_-(x))P(x,t)\right].$$

Substituting the quasistationary solution $p(x,t) = C_0 e^{-\lambda_0 t}\Pi(x)$ into (4.84) and using the fact that λ_0 is exponentially small give

$$J_0 = (\Omega_+(x) - \Omega_-(x))\Pi(x) - \frac{1}{2N}\frac{\partial}{\partial x}\left[(\Omega_+(x) + \Omega_-(x))\Pi(x)\right],$$

where J_0 is the constant flux through x_0. In a neighborhood of x_0, this equation can be Taylor expanded to leading order in $x - x_0$ and integrated to obtain the solution

$$\Pi(x) = \frac{J_0 N}{\Omega_+(x_0)} \mathrm{e}^{(x-x_0)^2/\sigma^2} \int_x^\infty \mathrm{e}^{-(y-x_0)^2/\sigma^2} dy, \tag{4.85}$$

where

$$\sigma = \sqrt{\frac{2\Omega_+(x_0)}{N[\Omega_+'(x_0) - \Omega_-'(x_0)]}} \tag{4.86}$$

determines the size of the boundary layer around x_0.

In order to match the activation and relaxation solutions, the following asymptotic behavior of the inner solution (4.85) is used:

$$\Pi(x) = \begin{cases} \dfrac{NJ_0\sigma^2}{(x-x_0)\Omega_+(x_0)}, & x - x_0 \gg \sigma \\ \dfrac{NJ_0\sigma\sqrt{\pi}}{\Omega_+(x_0)} \mathrm{e}^{(x-x_0)^2/\sigma^2}, & x_0 - x \gg \sigma. \end{cases} \tag{4.87}$$

The solution to the right of the saddle matches the relaxation solution (4.77) since $\Omega_+(x) - \Omega_-(x) \approx (x - x_0)[\Omega_+'(x_0) - \Omega_-'(x_0)]$ for $x \approx x_0$ such that $B = J_0$. In order to match the solution on the left-hand side of x_0 with the activation solution (4.76), Taylor expand $\Phi(x)$ about x_0 using $\Phi'(x_0) = 0$ and $\Phi''(x_0) = 2/N\sigma^2$. It follows that

$$J_0 = \frac{A\Omega_+(x_0)}{\sqrt{\Omega_+(x_0)\Omega_-(x_0)}} \sqrt{\frac{|\Phi''(x_0)|}{2\pi N}} \mathrm{e}^{-N\Phi(x_0)}. \tag{4.88}$$

The final step in the analysis is to link the flux J_0 with the escape rate λ_0. This is achieved by substituting the quasistationary solution into the continuity equation (4.84) and integrating over the interval $x \in [0, x_0]$ with a reflecting boundary condition at $x = 0$:

$$\frac{1}{\lambda_0} = \frac{1}{J_0} \int_0^{x_0} \phi^{\varepsilon}(y) dy. \tag{4.89}$$

Since the activation solution is strongly peaked around the fixed point x_-, a Gaussian approximation of $\phi^{\varepsilon}(x)$ around x_- yields the final result

$$\lambda_0 = \frac{\Omega_+(x_-)}{2\pi} \sqrt{|\Phi''(x_0)|\Phi''(x_-)} \mathrm{e}^{-N[\Phi(x_0)-\Phi(x_-)]}. \tag{4.90}$$

Hence, we obtain (4.63) with $\tau_i = \lambda_0^{-1}$ and

$$\Phi''(x) = \frac{d}{dx} \ln \left(\frac{\Omega_-(x)}{\Omega_+(x)} \right) = \frac{\Omega_-'(x)}{\Omega_-(x)} - \frac{\Omega_+'(x)}{\Omega_+(x)} = \gamma(x).$$

Similarly, we can obtain (4.64) for the mean time τ_f to terminate a spark.

4.4.4 Stochastic Phase-Plane Analysis

In the above analysis of Ca^{2+} sparks, the concentration c_{sr} in the JSR was held fixed. This is a reasonable approximation when considering the initiation of a Ca^{2+} spark. However, following Ca^{2+} release from the RyRs, the Ca^{2+} concentration c_{sr} slowly changes according to

$$\tau_{sr} \frac{dc_{\mathrm{sr}}}{dt} = -c_{sr}x + k_{sr}[c_0 - c_{\mathrm{sr}}]. \tag{4.91}$$

where $\tau_{sr} \gg \tau_{\mathrm{o}} \gg \tau_D$. The first term on the right-hand side is the loss of Ca^{2+} through the RyRs, whereas the second terms are the influx J_{SR} of Ca^{2+} from the NSR with fixed Ca^{2+} concentration c_0; see Fig. 4.4. The variation of c_{sr} means that one has to modify the analysis of the time to terminate the Ca^{2+} spark. Following Hinch [276], this can be achieved by combining the theory of stochastic transitions outlined in Sect. 4.4.2 with the classical phase-plane analysis of slow–fast excitable systems such as the FitzHugh–Nagumo equations (see Sect. 2.1). That is, (4.62) and (4.91) form an excitable system with the fraction x of open RyRs acting as the fast variable and c_{sr} acting as the slow variable. In Fig. 4.6 we sketch the nullclines of the deterministic system in a parameter regime where there is a single, stable fixed point (x^*, c_{sr}^*). In the full stochastic model, the initiation of a Ca^{2+} spark induces a transition to the right-hand x-nullcline according to $x_-(c_{sr}^*) \to x_+(c_{sr}^*)$ as outlined in Sect. 4.4.2. The slow variable then moves down the right-hand nullcline $x_+(c_{sr})$ according to the equation

$$\tau_{sr} \frac{dc_{\mathrm{sr}}}{dt} = -c_{sr}x_+(c_{sr}) + k_{sr}[c_0 - c_{\mathrm{sr}}]. \tag{4.92}$$

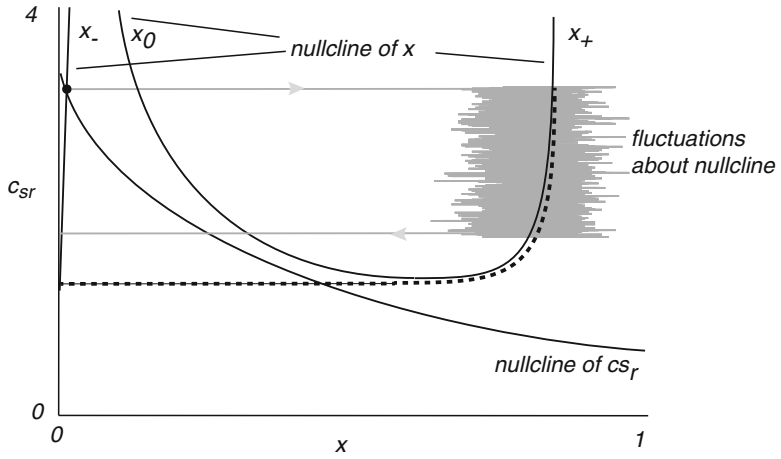

Fig. 4.6 Sketch of nullclines in the deterministic planar Ca^{2+} spark model with x denoting the fraction of open RyRs and c_{SR} the Ca^{2+} concentration in the junctional SR. The c_{sr} nullcline is a monotonically decreasing function $x(c_{sr})$, whereas the x nullcline is cubic-like with three branches $x_{\pm}(c_{sr})$ and $x_0(c_{sr})$. (Note that the branch $x_-(c_{sr}) \approx 0$; we have moved it away from the vertical axis for the sake of illustration.) In the given diagram there is a single, stable fixed point on the left-hand branch. In the stochastic version of the model a Ca^{2+} spark initiates a jump to the right-hand branch $x_+(c_{sr})$ along the lines outlined in Sect. 4.4.2. This is followed by a stochastic trajectory in which the slow variable $c_{sr}(t)$ moves down the nullcline until it undergoes a noise-induced transition back to the left-hand branch before the knee at $x = x_c$. In the deterministic case, the return transition occurs at the knee (*dashed curve*)

That is, although x is a stochastic variable, it fluctuates much faster than the dynamics of c_{sr} so one can substitute a time-averaged value of x in (4.91).

Suppose that $c_{sr}(t)$ is the solution of (4.92) with $c_{sr}(0) = c_{sr}^*$, that is, the Ca^{2+} spark occurs at $t = 0$. In principle, the spark can terminate at any time $t > 0$ due to fluctuations in the number of open RyRs. Again using a separation of time scales, we can estimate the rate of transition back to the left-hand branch at time t using

$$\lambda(t) = \frac{\Omega_+(x_+(t))\sqrt{|\gamma(x_0(t))|\gamma(x_+(t))}}{2\pi} e^{N[\Phi(x_+(t))-\Phi(x_0(t))]}, \tag{4.93}$$

where $x_+(t) = x_+(c_{sr}(t))$, etc. One can now calculate the distribution of spark durations T. Let $P(\tau) = \mathbb{P}(T > \tau)$ and introduce the spark duration probability density

$$p(\tau) = -\frac{dP}{d\tau}.$$

The probability that a spark terminates in an infinitesimal time interval $\delta\tau$ is $\lambda(\tau)\delta\tau$, so that

$$P(\tau + \delta\tau) = P(\tau)(1 - \lambda(\tau)\delta\tau).$$

Taking the limit $\delta\tau \to 0$ and integrating gives $P(\tau) = \exp\left(-\int_0^\tau \lambda(t)dt\right)$, and hence

$$p(\tau) = \lambda(\tau)\exp\left(-\int_0^\tau \lambda(t)dt\right). \tag{4.94}$$

4.4.5 Whole-Cell Model of Ca^{2+} Sparks

One of the major simplifications of the Hinch model [276] is that the background Ca^{2+} concentrations in the mytoplasm (c_m) and the NSR ($c_{\rm nsr}$) are held fixed. It thus fails to capture the collective behavior of a large population of Ca^{2+} release units (CaRUs) that are coupled via global changes in these background concentrations (assuming diffusion can be neglected on the relevant time scales). This has motivated the development of a whole-cell model of calcium-induced calcium release in cardiac myocytes, based on a system of $\mathcal{N}$ globally coupled CaRUs [672, 673]. We will describe a simplified version of the model in which Ca^{2+} pumps, leakage currents, and voltage-gated Ca^{2+} channels are not modeled explicitly. Let c_j and $\hat{c}_j$ denote the Ca^{2+} concentration in the dyadic space and JSR of the jth CaRU, $j = 1,\ldots,\mathcal{N}$. Then

$$\tau_D \frac{dc_j}{dt} = J^j_{\rm RyR} - J^j_{\rm D}, \qquad \tau_{sr}\frac{d\hat{c}_j}{dt} = J^j_{sr} - J^j_{\rm RyR}, \tag{4.95}$$

where $J^j_{\rm RyR}$ is the total Ca^{2+} current through the RyRs, $J^j_{\rm D}$ is the diffusive current from the diadic space of the jth CaRU to the bulk mytoplasm, and $J^j_{\rm sr}$ is the current from the NSR to the JSR of the jth CaRU. The various fluxes are given by

$$J^j_{\rm D} = c_j - c_m, \quad J^j_{\rm RyR} = x_j\hat{c}_j, \quad J^j_{sr} = k_{sr}[c_{\rm nsr} - \hat{c}_j], \tag{4.96}$$

where x_j is the fraction of open RyRs in the jth CaRU. Finally, from conservation of Ca^{2+} ions, the bulk concentrations c_m and $c_{\rm nsr}$ evolve according to

$$\tau_{\rm m}\frac{dc_m}{dt} = -\sum_{j=1}^{\mathcal{N}} J^j_D + J_m, \qquad \tau_{sr}\frac{dc_{\rm nsr}}{dt} = J_{\rm nsr} - \sum_{j=1}^{\mathcal{N}} J^j_{sr}. \tag{4.97}$$

Here J_m and $J_{\rm nsr}$ are the total external currents into the mytoplasm and NSR, respectively, arising from Ca^{2+} pumps and other factors.

When the number $\mathcal{N}$ of CaRUs is large, one can develop a probability density version of the above model, which takes the form of a differential Chapman–Kolmogorov (CK) equation describing the evolution of a single equivalent stochastic CaRU [672]. The basic idea is to introduce a probability density $p(c,\hat{c},n,t)$, with $p(c,\hat{c},n,t)dcd\hat{c}$ interpreted as the fraction of CaRUs at time t that have Ca^{2+} concentrations in the range $c \le c(t) \le c+dc, \hat{c} \le \hat{c}(t) \le \hat{c}+d\hat{c}$ and are in the internal state n, with the latter determined by the number of open RyRs, for example. Introduce the single CaRU equations

$$\tau_D \frac{dc}{dt} \equiv F(c,\hat{c},n) = \frac{n}{N}\hat{c} + c_m - c$$
$$\tau_{sr} \frac{d\hat{c}}{dt} \equiv \hat{F}(\hat{c},n) = k_{sr}[c_{\rm nsr} - \hat{c}] - \frac{n}{N}\hat{c}. \tag{4.98}$$

The probability density p then evolves as

$$\frac{\partial p}{\partial t} = -\frac{\partial (Fp)}{\partial c} - \frac{\partial (\hat{F}p)}{\partial \hat{c}} + \sum_{n'} A(n,n';c,\hat{c}) p(c,\hat{c},n',t), \tag{4.99}$$

with $A(n,n',c,\hat{c})$ constructed from the transition rates of the master equation describing the opening and closing of RyRs within each CaRU. Note that the CK equation (4.99) is formally similar to the CK equation (1.143) for membrane voltage fluctuations considered; see Sects. 1.5 and 1.6. However, the solution of (1.126) represents the distribution of state trajectories with respect to repeated trails of a single neuron, whereas the solution of (4.99) represents the distribution of state trajectories with respect to a large ensemble of identical CaRUs. Moreover, the latter are globally coupled due to the dependence of $F, \hat{F}$ and A on the Ca^{2+} concentrations $c_m, c_{\rm nsr}$. Within the probabilistic framework these evolve according to the equations

$$\tau_{\rm m} \frac{dc_m}{dt} = -\int_0^\infty \int_0^\infty \rho(c,\hat{c},t)[c_m - c] dc d\hat{c} + J_m \tag{4.100}$$
$$\tau_{sr} \frac{dc_{\rm nsr}}{dt} = J_{\rm nsr} - k_{sr} \int_0^\infty \int_0^\infty \rho(c,\hat{c},t)[c_{\rm nsr} - \hat{c}] dc d\hat{c}, \tag{4.101}$$

with $\rho(c,\hat{c},t) = \sum_n p(c,\hat{c},n,t)$. The probability density formulation of CaRUs can increase computational efficiency compared to Monte Carlo simulations of the full ODE model [672, 673].

4.5 Intercellular Calcium Waves in Astrocytes

So far we have considered intracellular Ca^{2+} waves that propagate within a single cell. However, one also finds intercellular Ca^{2+} waves (ICWs) consisting of increases in cytoplasmic Ca^{2+} concentration that are communicated between cells and appear as waves that spread out from an initiating or trigger cell. The speed and size of ICWs depend on the initiating stimulus and the particular propagation mechanism. An ICW often propagates at a speed of 10–20 μm/s and lasts for periods of up to tens of seconds, indicating that it can involve the recruitment of hundreds of contiguous cells. ICWs were first observed in cultures of astrocytes (discussed below) in response to extracellular glutamate [143], and in airway epithelial cells following mechanical stimulation [550]. They have subsequently been found in a wide range of cell types and under a variety of stimulus conditions, as reviewed in [380, 554].

4.5.1 Astrocytes and the Tripartite Synapse

Within the context of the central nervous system (CNS), ICWs are emerging as a major long-range signaling mechanism of a particular type of glial (nonneuronal) cell known as an *astrocyte*; see Fig. 4.7. Other types of glial cells include *oligodendrocytes* and *radial glial cells*. The former are responsible for myelination in the CNS just as Schwann cells are responsible for myelination in the peripheral nervous system; see also Sect. 2.5. On the other hand, radial glial cells play a pivotal role during development, with regard to both neuronal migration and neurogenesis [101]; see Sect. 9.1. Radial glial cells usually disappear post-development, but some cells, such as Bergmann glia in the cerebellum and Muller glia in the retina, maintain their radial glia-like properties into adulthood.

Traditionally, astrocytes were thought to be physiologically passive cells that only play a supporting role in the CNS by regulating and optimizing the environment within which neurons operate. Their housekeeping duties include maintaining local ion and pH homeostasis, delivering glucose and providing metabolic support via contacts with the vasculature, and clearing neuronal waste such as metabolic products and excess neurotransmitters in the synaptic cleft. However, over the past 20 years there has been an increasing amount of empirical data indicating that astrocytes play an active role in modulating synaptic transmission [253, 268, 449]. That is, astrocytes respond to synaptic neurotransmitters such as glutamate by elevating their intracellular Ca^{2+} levels. This then results in the release of glutamate and other signaling molecules from the astrocytes (gliotransmission), which in turn influences synaptic activity. Thus, astrocytes could potentially contribute to higher brain function and, consequently, behavior. This is consistent with the fact that the number of astrocytes relative to the number of neurons increases dramatically with

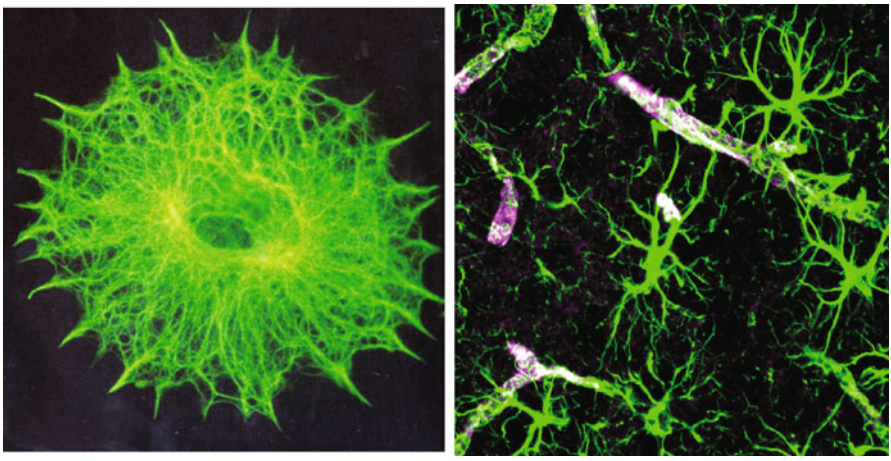

Fig. 4.7 *Left*: Astrocyte in vitro stained with GFAP to show filaments. *Right*: Astrocytes stained for GFAP, with end-feet ensheathing blood vessels [Public domain figure from Wikipedia Commons]

brain complexity, ranging from 1:25 in the leech, 1:6 in *C elegans*, 1:3 in lower mammals, to 1.4:1 in the human cortex. Conversely, it is known that following injury to the nervous system or under pathological conditions such as Alzheimer's disease, epilepsy, and schizophrenia, the structure and protein expression of astrocytes are altered [564]. One interpretation of these structural changes is that they are indicative of the supportive action of astrocytes following injury. On the other hand, given that many CNS disorders are correlated with alterations in synaptic transmission and gliotransmission regulates synaptic processing, it is possible that changes in gliotransmission contribute to these disorders; see Chap. 9.

In many higher organisms, astrocytes establish nonoverlapping anatomical and functional domains of size around 100 μm, and their distribution is highly organized.

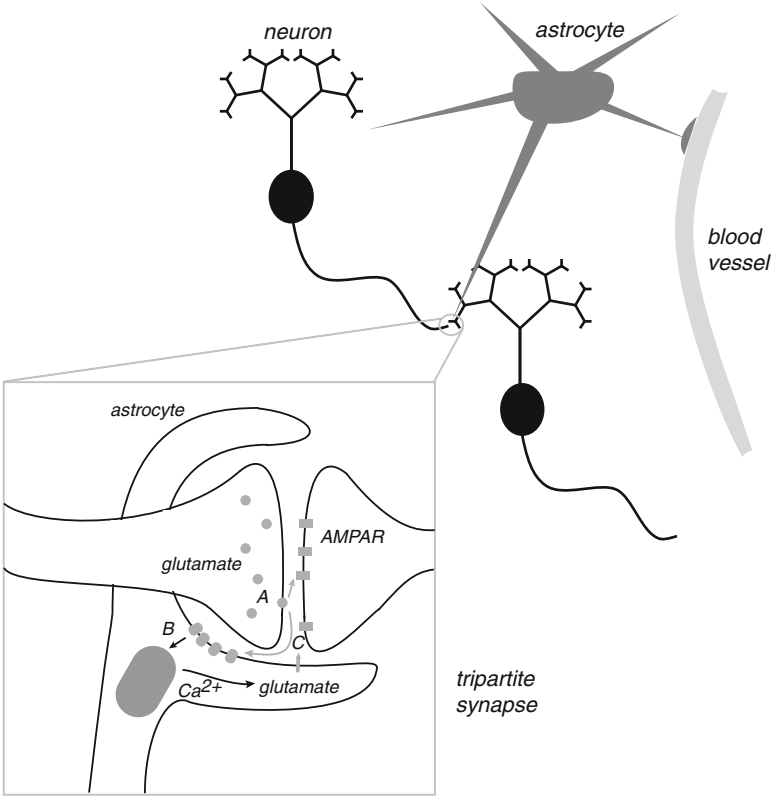

Fig. 4.8 Astrocytes modulate synaptic transmission and blood flow via Ca^{2+} signaling. *Inset*: the tripartite synapse. Synaptic transmission of glutamate (A) activates not only postsynaptic receptors such as AMPA but also astrocytic receptors that elevate astrocytic Ca^{2+} levels (B). This then induces the local release of glutamate from the astrocyte (C), which can modulate the synapse. Astrocytes also form a link between a neuron and the local vasculature. Increases in astrocytic Ca^{2+} concentration propagate via astrocyte end feet to small blood vessels, where they control vessel diameter and blood flow

The resulting astrocytic network parcellates the whole neutrophil such that a single astrocyte can make contact with thousands of synapses. The processes of a single astrocyte make contact with a synapse by wrapping around both the presynaptic and postsynaptic domains to form what is known as a *tripartite synapse* [253, 268, 449]; see Fig. 4.8. Hence, from a geometrical perspective, it is well placed to modulate synaptic transmission. The first component of glial–neuronal interactions at a synapse, namely, the metabotropic glutamate receptor 5 (mGluR5)-dependent elevation in astrocytic Ca^{2+} concentration in response to the release of glutamate neurotransmitters, was discovered in the early 1990s using Ca^{2+} imaging to study cultured glial cells [106, 143]. Both intracellular Ca^{2+} oscillations and ICWs propagating between neighboring astrocytes were observed. Subsequent studies have established that neuroglial signaling also occurs in astrocytes of isolated retina and brain slices [265, 460]. (Note, however, that a recent study of adult rodents has called into question the link between neuroglial Ca^{2+} signaling at the tripartite synapse [610]. It would appear that the astrocytic expression of mGluR5 receptors is developmentally regulated and, in particular, is undetectable in mature rodent brains; almost all previous studies of the tripartite synapse have been in immature animals.) Following the observation that neuronal activity increases Ca^{2+} levels in astrocytes, it was subsequently discovered that the resulting Ca^{2+} elevation induces gliotransmission of glutamate and a variety of other signaling molecules including ATP [249, 491]. Gliotransmission has been demonstrated to modulate synaptic transmission presynaptically and postsynaptically. For example, glutamate can enhance neurotransmitter release presynaptically by binding to metabotropic (mGlu) receptors or kainate receptors [189, 388]. Another example of enhanced synaptic transmission is the binding of ATP to postsynaptic receptors, which induces elevations in Ca^{2+}. This, in turn, can drive the insertion of additional AMPA receptors, thus temporarily increasing synaptic efficacy [236]. (The binding of ATP to postsynaptic receptors also provides a mechanism for the propagation of ICWs via paracrine signaling; see below.) On the other hand, hydrolysis of ATP results in the accumulation of adenosine, causing a reduction of synaptic transmission [493].

In addition to directly modulating synaptic transmission, astrocytes appear to regulate NMDA-receptor function. Recall from Sect. 1.3 that NMDA receptors are crucial for the induction of long-term synaptic plasticity, requiring both glutamate and postsynaptic depolarization in order to activate. The opening of an NMDA channel leads to a temporary increase of intracellular Ca^{2+} within the postsynaptic domain, whose amplitude and temporal profile determine whether the synapse is potentiated or depressed. It turns out that there is an additional glycine-binding site that regulates NMDA-receptor activity, whose co-agonist D-serine is released by astrocytes during gliotransmission. Increases in the level of D-serine appear to shift the balance point of long-term plasticity from depression to potentiation [485], a process known as metaplasticity. Finally, not only does astrocytic Ca^{2+} signaling modulate synaptic transmission and plasticity, it also controls blood flow, since intracellular waves propagate to small blood vessels via astrocyte end feet, where they control vessel diameter; see Fig. 4.8.

Following the original studies of ICWs in astrocyte cultures [106, 143], intracellular Ca^{2+} wave propagation between astrocytes has been observed in vitro in brain slices and whole retina preparations [265, 460, 492]. These empirical findings, combined with the structure of the tripartite synapse, have led to the suggestion that networks of astrocytes could form an extraneuronal pathway for rapid long-distance signaling within the CNS, which interacts reciprocally with neuronal networks. In particular, ICWs could provide a potential mechanism for coordinating and synchronizing the activity of a large group of neuronal and nonneuronal cells. It should be pointed out, however, that the function of ICWs in astrocytes remains controversial, since there have been very few in vivo observations of ICWs in the CNS, excluding the case of spontaneous ICWs during early development where astrocytes play a role in the generation, differentiation, and migration of neurons [666]; see Sect. 9.1. One recent exception is a study demonstrating in vivo spontaneous ICWs (termed glissandi) in mouse hippocampal astrocytes. (ICWs have also been observed in vivo in other glial networks, e.g., Bergmann glia in the cerebellum of rodents [287].) Another concern regarding the functional role of ICWs, either in vitro or in vivo, is whether they require strong inducing stimuli that do not have a normal physiological counterpart. On the other hand, certain pathological conditions such as brain trauma, brain ischemia (oxygen deprivation), and seizures are often associated with strong stimuli. They are all coupled with the release of ATP and glutamate and reductions in the level of extracellular Ca^{2+} that collectively could promote ICW generation. Such ICWs could exacerbate an injury by propagating signals that initiate

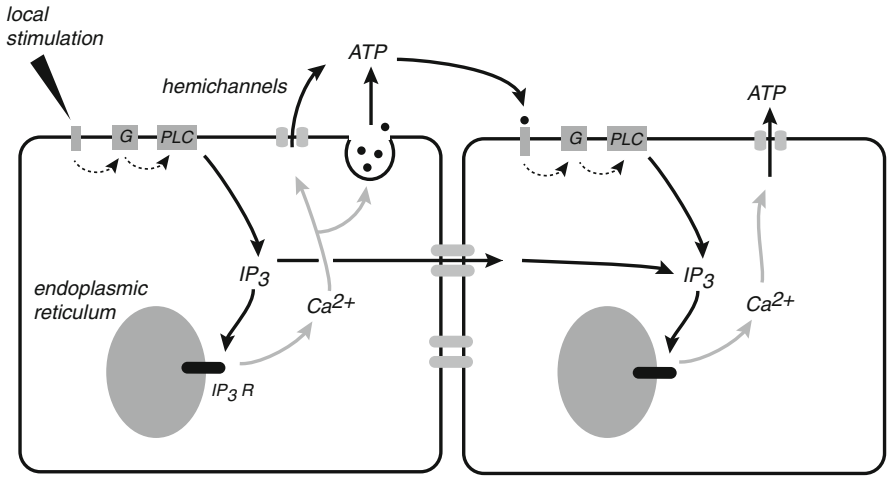

Fig. 4.9 Two mechanisms for the propagation of ICWs. Local stimulation of a single cell induces an elevation in intracellular IP_3 that generates an intracellular Ca^{2+} wave. Diffusion of IP_3 through gap-junction coupling with an adjacent cell initiates a second intracellular Ca^{2+} wave. In addition, or alternatively, stimulation of the first cell releases ATP via hemichannels in the plasma membrane or vesicular release; this could also be dependent on intracellular Ca^{2+}. The extracellular diffusion of ATP to neighboring cells can activate metabotropic receptors that then stimulate the production of IP_3 and the production of downstream intracellular Ca^{2+} waves

cell apoptosis (cell death) in surrounding cells [681]. There is also growing evidence that ICWs provide a source of excitation during epileptic episodes [564, 647, 668]; see Sect. 9.4. For example, studies of a brain slice that exhibits epileptiform activity, showed that there was also a corresponding increase in the frequency of Ca^{2+} oscillations in astrocytes [623]. Moreover, the release of glutamate from astrocytes has been observed to cause synchronous neuronal depolarizations [186].

4.5.2 Mechanisms and Models of Intercellular Calcium Waves

There are thought to be two basic mechanisms for the propagation of ICWs between adjacent cells that occur in astrocytes and other cell types: (a) diffusion of the second messenger IP_3 and, to a lesser extent, Ca^{2+} via gap junctions; (b) paracrine signaling via a diffusing extracellular messenger such as ATP. These mechanisms are illustrated in Fig. 4.9.

Gap-Junction Signaling

Gap junctions are arrays of transmembrane channels that connect the cytoplasm of two neighboring cells and thus provide a direct diffusion pathway between the cells. Cells sharing a gap-junction channel each provides a hemichannel (also known as a connexon) that connect head-to-head [545]. Each hemichannel is composed of proteins called connexins that exist as various isoforms named Cx23 through Cx62, with Cx43 being the most common. The physiological properties of a gap junction, including its permeability and gating characteristics, are determined by the particular connexins forming the channel. Although gap junctions are readily permeable to Ca^{2+} and IP_3, the diffusion of Ca^{2+} through a channel is greatly restricted due to buffering, so that the propagation of ICWs is primarily mediated by the diffusion of IP_3 when gap junctions are the main mechanism. The possible role of gap junctions in the propagation of ICWs was initially suggested by the observation in epithelial cells that waves only spread in adjacent cells from localized membrane sites in direct contact with the initiating cell. Moreover, the ICWs were not influenced by fluid flow over the apical surface of cells, that would have interfered with extracellular signals [259]. Further evidence for the role of gap junctions came from the study of glioma cells that lacked gap junctions [107]. These cells only supported ICWs when they were transfected with connexins; however, the presence of connexins could also enhance ATP and thus contribute to paracrine signaling (see below). Subsequent experimental and modeling studies have established that the diffusion of IP_3 through gap junctions can support the propagation of ICWs [379, 591]. In particular, ICWs could be initiated by an elevation of IP_3 in a single cell followed by diffusion to other cells without any regeneration of IP3. On the other hand, the range of the waves tends to be limited to only a few cells, suggesting that some other mechanism may be needed in order to generate longer-range waves.

The first model of ICWs mediated by gap junctions was based on studies of mechanical stimulation of cultured epithelial cells [590, 591]. It has subsequently been extended to models of ICWs in networks of astrocytes of varying complexity [163, 281, 310]. The models all have the same basic structure, but differ in terms of whether or not regenerative mechanisms or extracellular signaling mechanisms are included. A simple 1D version of an ICW model is shown in Fig. 4.10. Each cell is treated as a square of size L with local coordinates (x,y), $0 \le x,y \le L$. There are N cells labeled $n = 1,\ldots,N$ arranged on a regular lattice with nearest neighbor coupling. The intracellular dynamics within each cell is described by reaction–diffusion equations of the form given in Sect. 4.2. For example, in the original model of Sneyd et al. [591], this included equations for cytoplasmic Ca^{2+} concentration (c_n), IP_3 concentration p_n, and a slow variable h_n representing the fraction of IP3 receptors that have not been inactivated by Ca^{2+}. An example of an intracellular model for the nth cell is (see, e.g., [280])

$$\frac{\partial p_n}{\partial t} = D_p \nabla^2 p_n - k_p p_n, \tag{4.102a}$$

$$\frac{\partial c_n}{\partial t} = D_c \nabla^2 p_n - k_c c_n + f(c_n, h_n, p_n), \tag{4.102b}$$

$$\tau_h \frac{dh_n}{dt} = h_\infty(c_n) - h_n. \tag{4.102c}$$

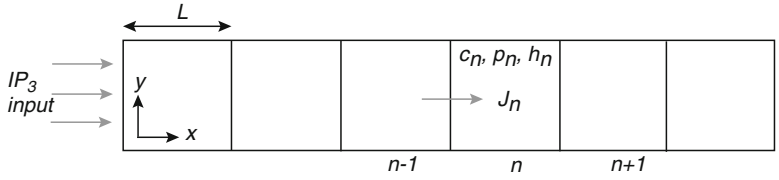

Fig. 4.10 Schematic diagram of a 1D model of intercellular Ca^{2+} waves mediated by gap junctions

Here the nonlinear function f represents the net flux due to Ca^{2+} release from IP_3 receptors. It is usually assumed that $D_p \gg D_c$ due to Ca^{2+} buffering. Coupling between adjacent cells in incorporated into the model using the boundary conditions for IP_3. Thus along the common vertical edge between cells $n-1$ and n, $1 < n < N$, the IP_3 flux J_n is taken to be of the form

$$-D_p \left.\frac{\partial p_{n-1}(x,y)}{\partial x}\right|_{x=L} = D_p \left.\frac{\partial p_n(x,y)}{\partial x}\right|_{x=0} \equiv \mathscr{K}[p_{n-1}(L,y) - p_n(0,y)]. \tag{4.103}$$

These are supplemented by no-flux boundary conditions for IP_3 across all other edges; all cell borders are assumed to be impermeable to Ca^{2+}. In a 2D version of the model arranged on a square grid, IP_3 can also flow across common horizontal

edges of neighboring cells, while no-flux boundary conditions are imposed along the exterior boundary of the grid. A typical simulation of such a model is to inject IP_3 in the cell at one end of the lattice, which is then allowed to diffuse from cell to cell, resulting in the propagation of an intracellular calcium wave. It is important to note that the ICW is not a traveling wave in the mathematical sense used throughout this book. Rather, the spread of Ca^{2+} is mediated by passive diffusion of intracellular Ca^{2+} and intra-/intercellular IP_3. Thus the rate of spread decreases with distance from the stimulated cell, and the arrival time of the wave increases exponentially with distance. In order to create more persistent ICWs, it is necessary to incorporate some regenerative mechanism. One example of such a mechanism is to assume that the rate of production of IP_3 can be amplified by intracellular Ca^{2+} so that (4.102a) becomes [281]

$$\frac{\partial p_n}{\partial t} = D_p \nabla^2 p_n + \frac{\nu c_n^2}{K + c_n^2} - k_p p_n.$$

Hofer et al. [281] showed that for an intermediate range of values of ν, partial regeneration of IP_3 supports ICWs that propagate further than those relying solely on passive diffusion of IP_3. Finally, an alternative mechanism for increasing the range of ICWs, which does not require some form of regeneration or active process, is to combine gap-junction coupling with an extracellular pathway involving ATP [163, 310]; see below.

Paracrine Signaling

Early evidence for the involvement of an extracellular component to ICWs arose from the observation that ICWs can propagate between disconnected groups of astrocytes, provided that the degree of separation does not exceed around 100 μm [266]. More recently, advanced imaging techniques have revealed that ICWs are associated with a cloud of extracellular ATP [249, 457]. There are a variety of pathways that could mediate ATP release, including hemichannels in the plasma membrane and vesicular discharge. Modeling studies suggest that a combination of gap-junction and paracrine signaling can significantly increase the range of ICWs [298]. It is also possible that there is a regenerative mechanism that boosts the propagation of ICWs. One candidate for active rather than passive (diffusive) wave propagation is Ca^{2+}-dependent ATP release via connexin hemichannels [652]. In the case of astrocytes, the dominant propagation mechanism depends on where they are located within the nervous system. For example, ICWs in the neocortex tend to be mediated by gap junctions, whereas in the hippocampus, both gap-junction and paracrine signaling play a role.

Here we will describe a mathematical model of paracrine signaling in astrocyte networks due to Bennett et al. [37]. Suppose that $a(t)$ denotes the extracellular concentration of ATP in the vicinity of a single cell. ATP binds to metabotropic P2Y receptors in the cell membrane according to the first-order kinetic scheme

$$ATP + R \underset{k_-}{\overset{k_+}{\rightleftharpoons}} R.$$

In the case of fast binding kinetics, the fraction of P2Y receptors that are bound by ATP is given by the quasi-equilibrium solution

$$r = \frac{a}{K_R + a}, \quad K_R = \frac{k_-}{k_+}. \tag{4.104}$$

This then drives activation of G-proteins according to the kinetic scheme

$$G_0 \underset{k_d}{\overset{k_a(r+r_0)}{\rightleftharpoons}} G_1,$$

where $G_{0,1}$ represent the inactive and active states of the G-protein. Denoting the amount of activated protein by g and the total G-protein by g_T, we have

$$\frac{dg}{dt} = k_a(r + r_0)(g_T - g) - k_d g. \tag{4.105}$$

Again assuming fast kinetics, the quasi-equilibrium solution is

$$g = g_T \frac{r + r_0}{K_G + r + r_0}, \quad K_G = \frac{k_d}{k_a}. \tag{4.106}$$

A major simplification of the model is to assume that the release of IP_3 within the cell is mainly driven by activation of G-protein so that Ca^{2+} dependence is ignored. If p is the intracellular IP_3 concentration then

$$\frac{dp}{dt} = \kappa g - k_{\text{deg}} p, \tag{4.107}$$

for constants κ, k_{deg}. The next stage of paracrine signaling, namely, the release of ATP by astrocytes is not yet well understood. However, IP_3 as a triggering mechanism, possibly via Ca^{2+} release from intracellular stores, is probably involved. In the model of Bennett et al. [37], IP_3 is assumed to directly cause ATP release from the cell surface into the extracellular space at the rate

$$J_{\text{ATP}}(p,t) = \kappa_{\text{ATP}} \chi(t) \left[\frac{p - p_{\min}}{K_{\text{rel}} + p} \right]_0. \tag{4.108}$$

Here κ_{ATP} and K_{rel} are constants, $[z]_0 = z$ for $z > 0$ and $[z]_0 = 0$ for $z < 0$, and $\chi(t)$ takes into account depletion of ATP stores within the cell. That is $\chi(0) = 1$ and

$$\frac{d\chi}{dt} = -\gamma J_{\text{ATP}}(t). \tag{4.109}$$

The rate of ATP release is thresholded in order to insure that very small levels of ATP are not amplified, and the depletion factor $\chi(t)$ is included in order to terminate

ATP release; the latter is motivated by the observation that ATP release is suppressed by repeated stimulation of a cell.

Finally, coupling between cells is modeled in terms of a diffusion equation for the extracellular ATP concentration that takes into account the IP_3-mediated release of ATP from the astrocytes. One way to proceed would be to use a continuum bidomain model, in which astrocytes and extracellular ATP coexist at every point in space. Taking $a = a(\mathbf{x},t), p = p(\mathbf{x},t)$ and denoting the density of astrocytes by $\rho(\mathbf{x})$, we would then have

$$\frac{\partial a}{\partial t} = D_{\rm ATP}\nabla^2 a + \rho(\mathbf{x})J_{\rm ATP}(p,t) - \frac{a}{K_{\rm deg}+a}. \tag{4.110}$$

Alternatively, one could explicitly distinguish between extracellular space and the intracellular space of astrocytes, in which case the fluxes $J_{\rm ATP}$ only exist at the boundaries of the cells. The latter approach is used in the computer simulations of Bennett et al. [37], who take a simplified cubic geometry for the astrocytes and also allow for intracellular diffusion of IP_3. Note that under a quasi-steady-state approximation, (4.107) and (4.110) form a closed system of differential equations, since (4.104) and (4.107) can be used to express g in terms of a. Hence, one can solve for the ATP and IP_3 concentrations independently of Ca^{2+} and then incorporate ICWs by using the IP_3 to drive a standard model of Ca^{2+} release from intracellular stores such as Li–Rinzel. However, if there is regenerative Ca^{2+}-dependent production of IP_3 or a Ca^{2+}-dependent mechanism for gliotransmission of ATP, then it is necessary to couple the Ca^{2+} dynamics to that of IP_3 and ATP.

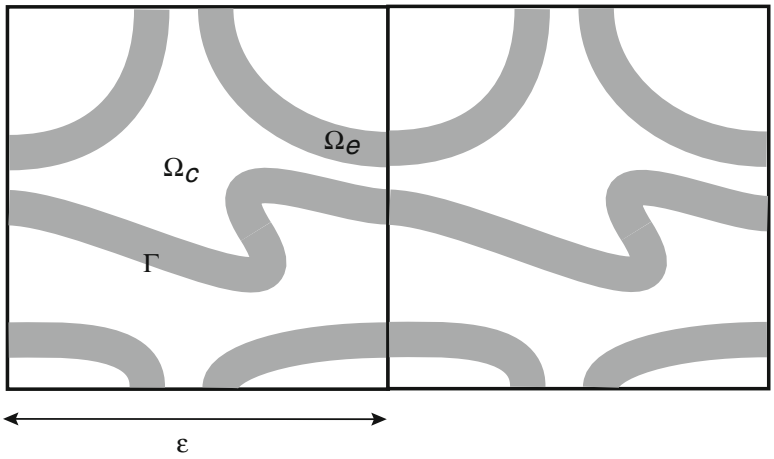

Fig. 4.11 Illustration of a 2D periodic heterogeneous medium consisting of a cytosolic domain Ω_c and an ER domain Ω_e separated by a boundary Γ

4.6 Appendix: Homogenization

As we noted in Sect. 4.2, it is not practical to try modeling the detailed microstructure of the cytoplasmic and ER boundaries, which are highly interleaved. This motivates consideration of a mean-field description of the Ca^{2+} concentrations, in which the concentrations c, c_e are taken to coexist at every point in space with effective diffusion coefficients. As shown by Goel et al. [224], the resulting bidomain model can be derived from first principles using homogenization theory. In this appendix we sketch the basic steps in their derivation. Note that we also encountered a 1D example of homogenization theory in Sect. 3.2.3, where we spatially averaged over a discrete distribution of dendritic spines.

Consider a domain $\Omega \subset \mathbb{R}^3$ in which the ER is treated as a periodic network that occupies a fraction of Ω, as illustrated in Fig. 4.11. For simplicity, assume that the unit cell is a cube of length ε. The ER Ca^{2+} occupies a connected domain Ω_e^ε, and the complementary connected domain $\Omega_c^\varepsilon = \Omega / \Omega_e^\varepsilon$ is occupied by cytosolic Ca^{2+}. The concentrations c^ε and c_e^ε satisfy the 3D diffusion equation in their respective domains:

$$\frac{\partial c}{\partial t} = \nabla \cdot (A_\varepsilon(\mathbf{x}/\varepsilon)\nabla c(\mathbf{x})), \quad \mathbf{x} \in \Omega_c^\varepsilon \tag{4.111a}$$

$$\frac{\partial c_e}{\partial t} = \nabla \cdot (B_\varepsilon(\mathbf{x}/\varepsilon)\nabla c_e(\mathbf{x})), \quad \mathbf{x} \in \Omega_e^\varepsilon, \tag{4.111b}$$

where A_ε and B_ε are the diffusion tensors for Ca^{2+} in the cytosol and ER, respectively. The boundary conditions on the membrane Γ_ε separating the cytosol from the ER take the form

$$A_\varepsilon(\mathbf{x}/\varepsilon)\nabla c(\mathbf{x}) \cdot \mathbf{n}_c^\varepsilon = \varepsilon f(c^\varepsilon, c_e^\varepsilon), \quad \text{on} \, \Gamma_\varepsilon \tag{4.112a}$$

$$-B_\varepsilon(\mathbf{x}/\varepsilon)\nabla c_e(\mathbf{x}) \cdot \mathbf{n}_c^\varepsilon = \varepsilon f(c^\varepsilon, c_e^\varepsilon), \quad \text{on} \, \Gamma_\varepsilon, \tag{4.112b}$$

where $n_c^\varepsilon, n_e^\varepsilon$ denote the unit exterior normals to the boundaries $\partial\Omega_c^\varepsilon$ and $\partial\Omega_e^\varepsilon$, respectively, satisfying $n_c^\varepsilon = -n_e^\varepsilon$ on Γ_ε, and f determines the net flux from the ER to the cytosol.

The basic idea of the homogenization method is to supplement the macroscopic spatial variables $\mathbf{x} = (x_1, x_2, x_3)$ with a set of microscopic variables $\mathbf{y} = (y_1, y_2, y_3), 0 \le y_i \le 1$, that are the coordinates of a unit cube [496, 630]. Denote by Ω_c (Ω_e) the set of points $y = x/\varepsilon$ in the unit cube for which $\mathbf{x} \in \Omega_c^\varepsilon$ ($\mathbf{x} \in \Omega_e^\varepsilon$). The concentrations $c^\varepsilon, c_e^\varepsilon$ are then taken to be functions of x and y with $\mathbf{x} \in \Omega, \mathbf{y} \in \Omega_c$ for c^ε, and $\mathbf{x} \in \Omega, \mathbf{y} \in \Omega_e$ for c_e^ε:

$$c^\varepsilon = c(\mathbf{x}, \mathbf{y}, t), \quad c_e^\varepsilon = c_e(\mathbf{x}, \mathbf{y}, t) \tag{4.113}$$

with $y = x/\varepsilon$. The next step is to introduce formal asymptotic expansion for c^ε and c_e^ε of the form

$$c^\varepsilon = c^0(\mathbf{x}, \mathbf{y}, t) + \varepsilon c^1(x, y, t) + \varepsilon^2 c^2(\mathbf{x}, \mathbf{y}, t) + \ldots \tag{4.114a}$$

$$c_e^\varepsilon = c_e^0(\mathbf{x}, \mathbf{y}, t) + \varepsilon c_e^1(\mathbf{x}, \mathbf{y}, t) + \varepsilon^2 c_e^2(\mathbf{x}, \mathbf{y}, t) + \ldots, \tag{4.114b}$$

where c^k and c_e^k are 1-periodic functions of $\mathbf{y}$. Setting

$$\nabla u = \nabla_{\mathbf{x}} u(\mathbf{x},\mathbf{y}) + \varepsilon^{-1}\nabla_{\mathbf{y}} u(\mathbf{x},\mathbf{y}),$$

it follows that (4.111) becomes

$$\frac{\partial c^\varepsilon}{\partial t} = \left(\varepsilon^{-2}\nabla_{\mathbf{y}}\cdot(A_\varepsilon(\mathbf{y})\nabla_{\mathbf{y}}) + \varepsilon^{-1}[\nabla_{\mathbf{x}}\cdot(A_\varepsilon(\mathbf{y})\nabla_{\mathbf{y}}) + \nabla_{\mathbf{y}}\cdot(A_\varepsilon(\mathbf{y})\nabla_{\mathbf{x}})] + A_\varepsilon(\mathbf{y})\nabla_{\mathbf{x}}^2\right) c^\varepsilon$$
$$\text{for}\,\mathbf{x}\in\Omega,\mathbf{y}\in\Omega_c \tag{4.115a}$$

$$\frac{\partial c_e^\varepsilon}{\partial t} = \left(\varepsilon^{-2}\nabla_{\mathbf{y}}\cdot(B_\varepsilon(\mathbf{y})\nabla_{\mathbf{y}}) + \varepsilon^{-1}[\nabla_{\mathbf{x}}\cdot(B_\varepsilon(\mathbf{y})\nabla_{\mathbf{y}}) + \nabla_{\mathbf{y}}\cdot(B_\varepsilon(\mathbf{y})\nabla_{\mathbf{x}})] + A_\varepsilon(\mathbf{y})\nabla_{\mathbf{x}}^2\right) c_e^\varepsilon$$
$$\text{for}\,\mathbf{x}\in\Omega,\mathbf{y}\in\Omega_e, \tag{4.115b}$$

and the boundary conditions (4.112) become

$$A_\varepsilon(\mathbf{y})\left[\nabla_{\mathbf{x}}+\varepsilon^{-1}\nabla_{\mathbf{y}}\right]c\cdot\mathbf{n}_c^\varepsilon = \varepsilon f(c^\varepsilon,c_e^\varepsilon), \quad \text{for}\,\mathbf{x}\in\Omega,\mathbf{y}\in\Gamma_\varepsilon \tag{4.116a}$$

$$-B_\varepsilon(\mathbf{y})\left[\nabla_{\mathbf{x}}+\varepsilon^{-1}\nabla_{\mathbf{y}}\right]c_e\cdot\mathbf{n}_c^\varepsilon = \varepsilon f(c^\varepsilon,c_e^\varepsilon), \quad \text{for}\,\mathbf{x}\in\Omega,\mathbf{y}\in\Gamma_\varepsilon. \tag{4.116b}$$

Substituting the asymptotic expansions for c^ε and c_e^ε and collecting terms of the same order in ε then yields a hierarchy of equations for c^k, c_e^k. At $\mathcal{O}(\varepsilon^{-2})$, we have

$$\nabla_{\mathbf{y}}\cdot(A_\varepsilon(\mathbf{y})\nabla_{\mathbf{y}})c^0 = 0, \quad \mathbf{y}\in\Omega_c \tag{4.117a}$$

$$\nabla_{\mathbf{y}}\cdot(B_\varepsilon(\mathbf{y})\nabla_{\mathbf{y}})c_e^0 = 0, \quad \mathbf{y}\in\Omega_e. \tag{4.117b}$$

together with the boundary conditions

$$A_\varepsilon(\mathbf{y})\nabla_{\mathbf{y}}c\cdot\mathbf{n} = 0 = B_\varepsilon(\mathbf{y})\nabla_{\mathbf{y}}c_e^0\cdot\mathbf{n}, \quad \mathbf{y}\in\Gamma, \tag{4.118}$$

where $\mathbf{n}$ is a unit normal on Γ. For fixed x, the only periodic solution to these equations is $c^0 = \text{constant}, c_e^0 = \text{constant}$, that is,

$$c^0 = c^0(x,t), \quad c_e^0 = c_e^0(x,t). \tag{4.119}$$

The $\mathcal{O}(\varepsilon^{-1})$ equations are

$$\nabla_{\mathbf{y}}\cdot\left(A_\varepsilon(\mathbf{y})\left[\nabla_{\mathbf{x}}c^0+\nabla_{\mathbf{y}}c^1\right]\right) = 0, \quad \mathbf{y}\in\Omega_c \tag{4.120a}$$

$$\nabla_{\mathbf{y}}\cdot\left(B_\varepsilon(\mathbf{y})\left[\nabla_{\mathbf{x}}c_e^0+\nabla_{\mathbf{y}}c_e^1\right]\right) = 0, \quad \mathbf{y}\in\Omega_e, \tag{4.120b}$$

together with the boundary conditions

$$A_\varepsilon(\mathbf{y})[\nabla_{\mathbf{x}}c^0+\nabla_{\mathbf{y}}c^1]\cdot\mathbf{n} = 0 = B_\varepsilon(\mathbf{y})[\nabla_{\mathbf{x}}c_e^0+\nabla_{\mathbf{y}}c_e^1]\cdot\mathbf{n}, \quad \mathbf{y}\in\Gamma. \tag{4.121}$$

The solutions for c^1 and c_e^1 can be written in the form

$$c^1(x,y,t) = \sum_{i=1}^{3} V_i^c(y)\frac{\partial c^0(x,t)}{\partial x_i} + \bar{c}^1(x,t), \tag{4.122a}$$

$$c_e^1(x,y,t) = \sum_{i=1}^{3} V_i^e(y) \frac{\partial c_e^0(x,t)}{\partial x_i} + \bar{c}_e^1(x,t), \tag{4.122b}$$

with the 1-periodic vectors $\mathbf{V}^c$ and $\mathbf{V}^e$ satisfying the "cell equations"

$$\nabla_{\mathbf{y}} \cdot (A_\varepsilon(\mathbf{y}) [\nabla_{\mathbf{y}} V_k^c(\mathbf{y}) + \mathbf{e}_k]) = 0, \quad \mathbf{y} \in \Omega_c \tag{4.123a}$$
$$\nabla_{\mathbf{y}} \cdot (B_\varepsilon(\mathbf{y}) [\nabla_{\mathbf{y}} V_k^e(\mathbf{y}) + \mathbf{e}_k]) = 0, \quad \mathbf{y} \in \Omega_e, \tag{4.123b}$$

and

$$A_\varepsilon(\mathbf{y})[\nabla_{\mathbf{y}} V_k^c(\mathbf{y}) + \mathbf{e}_k] \cdot \mathbf{n} = 0 = B_\varepsilon(\mathbf{y})[\nabla_{\mathbf{y}} V_k^e(\mathbf{y}) + \mathbf{e}_k] \cdot \mathbf{n}, \quad \mathbf{y} \in \Gamma, \tag{4.124}$$

for $k = 1,2,3$, where $\mathbf{e}_k$ is the vector with components $e_{jk} = \delta_{jk}$.

In order to derive mean-field equations for the homogenized concentrations c^0, c_e^0, it is necessary to proceed to $\mathscr{O}(1)$, for which

$$\nabla_{\mathbf{x}} \cdot \left[A_\varepsilon(\mathbf{y})(\nabla_{\mathbf{x}} c^0 + \nabla_{\mathbf{y}} c^1)\right] + \nabla_{\mathbf{y}} \cdot \left[A_\varepsilon(\mathbf{y})(\nabla_{\mathbf{x}} c^1 + \nabla_{\mathbf{y}} c^2)\right] = \frac{\partial c^0}{\partial t}, \quad \mathbf{y} \in \Omega_c \tag{4.125a}$$

$$\nabla_{\mathbf{x}} \cdot \left[B_\varepsilon(\mathbf{y})(\nabla_{\mathbf{x}} c_e^0 + \nabla_{\mathbf{y}} c_e^1)\right] + \nabla_{\mathbf{y}} \cdot \left[B_\varepsilon(\mathbf{y})(\nabla_{\mathbf{x}} c_e^1 + \nabla_{\mathbf{y}} c_e^2)\right] = \frac{\partial c_e^0}{\partial t}, \quad \mathbf{y} \in \Omega_e \tag{4.125b}$$

with boundary conditions

$$A_\varepsilon(\mathbf{y})[\nabla_{\mathbf{x}} c^1 + \nabla_{\mathbf{y}} c^2] \cdot \mathbf{n} = f(c^0, c_e^0), \quad \mathbf{y} \in \Gamma \tag{4.126a}$$
$$B_\varepsilon(\mathbf{y})[\nabla_{\mathbf{x}} c^1 + \nabla_{\mathbf{y}} c^2] \cdot \mathbf{n} = -f(c^0, c_e^0), \quad \mathbf{y} \in \Gamma. \tag{4.126b}$$

Integrating (4.125a) over Ω_c gives

$$\int_{\Omega_c} \left(\nabla_{\mathbf{x}} \cdot \left[A_\varepsilon(\mathbf{y})(\nabla_{\mathbf{x}} c^0 + \nabla_{\mathbf{y}} c^1)\right] + \nabla_{\mathbf{y}} \cdot \left[A_\varepsilon(\mathbf{y})(\nabla_{\mathbf{x}} c^1 + \nabla_{\mathbf{y}} c^2)\right]\right) d\mathbf{y} = |\Omega_c| \frac{\partial c^0}{\partial t}, \tag{4.127}$$

where $|\Omega_c|$ is the volume fraction of the unit cell occupied by the cytosol. Using (4.122a), the first term on the left-hand side becomes

$$\begin{aligned}
&\int_{\Omega_c} \nabla_{\mathbf{x}} \cdot \left[A_\varepsilon(\mathbf{y})(\nabla_{\mathbf{x}} c^0 + \nabla_{\mathbf{y}} c^1)\right] d\mathbf{y} \\
&= \int_{\Omega_c} \nabla_{\mathbf{x}} \cdot \left[A_\varepsilon(\mathbf{y})(\nabla_{\mathbf{x}} c^0 + \nabla_{\mathbf{y}} \left(\sum_{i=1}^{3} V_i^c(y) \frac{\partial c^0}{\partial x_i}\right)\right] d\mathbf{y} \\
&= \nabla_{\mathbf{x}} \cdot \left(\tilde{A}_\varepsilon \nabla_{\mathbf{x}} c^0\right),
\end{aligned}$$

where

$$[\tilde{A}_\varepsilon]_{ik} = \int_{\Omega_c} \sum_j [A_\varepsilon(\mathbf{y})]_{ij} \left[\frac{\partial V_k^c(\mathbf{y})}{\partial y_j} + \delta_{j,k}\right] d\mathbf{y}. \tag{4.128}$$

Finally, applying the divergence theorem to the second term on the left-hand side of (4.127),

$$\begin{aligned}\int_{\Omega_c} \nabla_{\mathbf{y}} \cdot \left[A_\varepsilon(\mathbf{y})(\nabla_{\mathbf{x}} c^1 + \nabla_{\mathbf{y}} c^2)\right] d\mathbf{y} &= \int_\Gamma A_\varepsilon(\mathbf{y})(\nabla_{\mathbf{x}} c^1 + \nabla_{\mathbf{y}} c^2) \cdot \mathbf{n} d\Gamma(\mathbf{y}) \\ &= \int_\Gamma f(c^0, c_e^0) d\Gamma(y) \\ &= |\Gamma| f(c^0, c_e^0).\end{aligned}$$

Combining all of the results, we obtain a macroscopic equation for c^0 given by

$$|\Omega_c| \frac{\partial c^0}{\partial t} = \nabla_{\mathbf{x}} \cdot \left(\tilde{A}_\varepsilon \nabla_{\mathbf{x}} c^0\right) + |\Gamma| f(c^0, c_e^0). \tag{4.129}$$

Proceeding in an identical fashion, we also obtain a macroscopic equation for c_e^0:

$$|\Omega_e| \frac{\partial c_e^0}{\partial t} = \nabla_{\mathbf{x}} \cdot \left(\tilde{B}_\varepsilon \nabla_{\mathbf{x}} c_e^0\right) - |\Gamma| f(c^0, c_e^0), \tag{4.130}$$

where $\tilde{B}_\varepsilon$ is defined according to (4.128) with A_ε replaced by B_ε on the right-hand side. Equations (4.129) and (4.130) constitute a bidomain model with homogenized diffusion tensors $\tilde{A}_\varepsilon$ and $\tilde{B}_\varepsilon$. The latter can be determined by solving the cell equations (4.123) and (4.124) for $\mathbf{V}^c$ and $\mathbf{V}^e$. Goel et al. [224] calculated effective diffusion tensors for several different ER microstructures. They found that diffusion in the cytoplasm could be halved as the ER volume fraction increased from 0 to 0.9.